

Accepted and scheduled for publication in *The Astrophysical Journal*, for the February 2012, v 745, 1st issue

## GX 3+1: the stability of spectral index as a function of mass accretion rate

Elena Seifina<sup>1</sup> and Lev Titarchuk<sup>2</sup>

### ABSTRACT

We present an analysis of the spectral and timing properties observed in X-rays from neutron star binary GX 3+1 (4U 1744-26) during long-term transitions between the *faint* and *bright* phases superimposed on short-term transitions between *lower banana* (LB) and *upper banana* (UB) branches in terms of its color-color diagram. We analyze all observations of this source obtained with the *Rossi* X-ray Timing Explorer and *BeppoSAX* satellites. We find that the X-ray broad-band energy spectra during these spectral transitions can be adequately reproduced by a composition of a low-temperature blackbody component, a Comptonized component (*COMPTB*) and *Gaussian* component. We argue that the electron temperature  $kT_e$  of the Compton cloud monotonically increases from 2.3 keV to 4.5 keV, when GX 3+1 makes a transition from UB to LB. We also detect an evolution of noise components (a very low frequency noise and a high frequency noise) during these LB – UB transitions. Using a disk *seed* photon normalization of *COMPTB*, which is proportional to the mass accretion rate, we find that the photon power-law index  $\Gamma$  is almost constant ( $\Gamma = 2.00 \pm 0.02$ ) when mass accretion rate changes by factor 4. In addition, we find that the emergent spectrum is dominated by the strong Comptonized component. We interpret this quasi-stability of the index  $\Gamma$  and a particular form of the spectrum in the framework of a model in which the energy release in the transition layer located between the accretion disk and neutron star surface dominates that in the disk. Moreover, this index stability effect now established for

---

<sup>1</sup>Moscow State University/Sternberg Astronomical Institute, Universitetsky Prospect 13, Moscow, 119992, Russia; seif@sai.msu.ru

<sup>2</sup>Dipartimento di Fisica, Università di Ferrara, Via Saragat 1, I-44100 Ferrara, Italy, email:titarchuk@fe.infn.it; George Mason University, School of Physics, Astronomy and Computational Sciences (SPACS), Fairfax, VA 22030 ltitarch@gmu.edu; Goddard Space Flight Center, NASA, code 663, Greenbelt MD 20770, USA; email:lev@milkyway.gsfc.nasa.gov, USA

GX 3+1 was previously found in the *atoll* source 4U 1728-34 and suggested for a number of other low mass X-ray neutron star binaries (see Farinelli & Titarchuk). This intrinsic behavior of neutron stars, in particular for *atoll* sources, is fundamentally different from that seen in black hole binary sources where the index monotonically increases during spectral transition from the low state to the high state and then finally saturates at high values of mass accretion rate.

*Subject headings:* accretion, accretion disks—neutron star physics—black hole physics—stars: individual (GX 3+1, 4U 1728-34):radiation mechanisms: nonthermal—physical data and processes

## 1. Introduction

Low mass X-ray binaries (LMXB) hosting a neutron star (NS) show a variety of spectral states and transitions between them. In this regard, the so-called *atoll* sources [see e.g. Hasinger & van der Klis (1989), van der Klis (2005)] are particularly interesting because they demonstrate a wide range of luminosities [the most of them show from 0.01 to 0.5 of the Eddington limit  $L_{Edd}$ ]. It is worth noting that the name of *atoll* sources is associated with the shape traced in the color-color diagram (CD). This shape can be divided into two main regions, corresponding to two X-ray states of the source: the harder one is related to the island (IS) state and the softer one is related to the banana (B) state.

These spectra of NS sources can be described by *blackbody* (BB) components, with color temperatures  $kT_{BB} < 1$  keV and  $kT_s > 1$  keV that are presumably related to the accretion disk and NS surface respectively. In addition, there is a thermal Comptonization component with electron temperature  $kT_e = 2.3 - 15$  keV that is probably related to the transition layer (TL) located between the disk and NS [see Paizis et al. (2006); Farinelli & Titarchuk (2011); Seifina & Titarchuk (2011), hereafter FT11 and ST11 respectively]. An analysis of X-ray power spectra of *atoll* sources indicates to a tight relation between timing properties and the position on the CD, suggesting that the source timing and spectral properties are well determined by basic parameter such as mass accretion rate [see, e.g., Di Salvo et al. (2001)].

GX 3+1 is one of the brightest *atoll* sources associated with a bulge component of our Galaxy. GX 3+1 along with GX 9+9, GX 9+1 and GX 13+1 form the subclass of persistently bright *atoll* sources, which are always in the banana state [see Hasinger & van der Klis (1989)]. In particular, two-branch structures have been observed in the CD and hardness-intensity diagram (HID) of GX 3+1 [Stella et al. (1985); Lewin et al. (1987); Schultz et al.

(1989); Homan et al. (1998); Munro et al. (1994); Schnerr et al. (2003)]. Specifically, their tracks in the X-ray CD are long, diagonal and slightly curved, while their fast timing properties are dominated only by a relatively weak (1 – 4% rms) power-law shaped noise component. These aforementioned atoll sources are intermediate in terms of luminosity that changes in the range 0.1-0.5 of  $L_{Edd}$  [see Christian & Swank (2006) and Ford & van der Klis (2000)].

In contrast to other atoll sources and Z sources, these bright atoll sources have so far not shown kHz QPOs [see Wijnands et al., (1998); Strohmayer (1998); Homan et al. (1998); Oosterbroek et al. (2001); Schnerr et al. (2003)], which can be attributed to the fact that these objects do not reach the *left lower banana* (LLB), where other atoll sources exhibit kHz QPOs [van der Klis (2000)]. For example, the weaker atoll sources, such as e.g. 4U 1608-52, 4U 0614+09 or 4U 1728-34, show kHz QPOs in LLB.

X-ray data of GX 3+1 (4U 1744-26) obtained in broad energy ranges using *BeppoSAX* (0.1 – 200 keV) and *RXTE* (3 – 200 keV) offer a unique possibility to further investigate, in detail, the evolution of X-ray spectral properties during transition events. This bright *atoll* source shows long-term transitions from the *fainter phase* to its *brighter phase* in X-rays and vice versa when the corresponding luminosity changes, at least, by a factor of 4, while on time scales of hours GX 3+1 demonstrates low flux variabilities as transitions between LB and UB states. Naturally one can pose a fair question: what is the physical mechanism responsible for the source emission during these luminosity changes and particularly how the spectral index changes during these transitions?

GX 3+1 was discovered during an *Aerobee*-rocket flight on June 16, 1964 (Bowyer et al. 1965). Subsequently, this source was observed many times during various observational campaigns. Detailed long-term monitoring observations of GX 3+1 was performed by *All Sky Monitor* on *GINGA* [see Asai et al. (1993)]; *EXOSAT* [see Schultz et al. (1989)]; *RXTE* [see Bradt et al. (1993); Kuulkers & van der Klis (2000)], *Wide Field Camera* (WFC) of *BeppoSAX* [see den Hartog et al. (2003)] and also by *INTEGRAL* [see Paizis et al. (2006)]. In particular, den Hartog et al. (2003) found three types of variability: *short-term* variation (of order of seconds), *mild* variability on a daily (hourly) time scale and *slow* sinusoidal-like variation on a time scale of years. However, it is surprising that the hardness ratio, which can be a measure of the spectral shape, stays almost constant during these observations.

Although an optical counterpart has not yet been identified [e.g. Naylor et al., (1991)] GX 3+1 is presumably a low mass X-ray binary in which a neutron star is accompanied by a low-mass star of spectral type A or a later. During an active stage the companion overflows its Roche lobe and transfers matter onto the NS via an accretion disk. This process is possibly accompanied by nuclear burning of helium or hydrogen layer of NS surface as a result of the matter accumulation on the NS surface (Hanson & van Horn 1975). Unstable

fusion occurs leading to thermonuclear flashes which can be observable in the form of X-ray bursts, so-called type-I X-ray bursts (Woosley & Taam 1976). GX 3+1 does exhibit fast variability in the form of type-I X-ray bursts, which were extensively studied by a number of X-ray missions *GINGA* (Asai et al. 1993), *Granat* [Pavlinisky et al. (1994), Molkov et al., (1999)] and by *RXTE* [Kuulkers & van der Klis (2000) and Kuulkers (2002)] and by INTEGRAL (Chenevez et al. 2006).

A unique super-burst with a decay time of 1.6 hours was detected with the All Sky Monitor (ASM) on *RXTE* (Kuulkers 2002). One of the shortest bursts ever seen exhibits a quick (i.e., less than 2 seconds) radius expansion phase, indicating that the burst luminosity was at the Eddington luminosity, causing the NS atmosphere to expand due to radiation pressure. This implies a distance to the source is about 4.5 kpc, assuming that the NS atmosphere is hydrogen-rich [see more details in Kuulkers & van der Klis (2000)].

In this Paper we concentrate our efforts on the spectral and timing properties of GX 3+1 related to changes in mass accretion rate, which are seen as the *mild* and *slow* variabilities. Previously, an analysis of the burst properties of GX 3+1 as a function of mass accretion rate on the time scales larger than one minute were presented by Asai et al. (1993) and den Hartog et al. (2003). In particular, the *slow* variability has been revealed during transitions from the *faint phase* to the *bright phase* of luminosity and are generally caused by significant increase of mass accretion rate. The *mild* variability is presumably related to moderate local variability of mass accretion rate and revealed as local transitions between *lower banana* and *upper banana* states. The *slow* variability has been investigated with the *RXTE*/ASM light curve, *Wide Field Camera* (WFC) of *BeppoSAX* (den Hartog et al. 2003) and the all sky monitor on *GINGA* (Asai et al. 1993) and these observations indicate that the flux oscillates semi-sinusoidally with a period of 6 – 7 years (see Fig. 1).

Moreover, the *GINGA* measurements with its Large Area Detector (Asai et al. 1993) show a constant 1 – 20 keV spectral shape over the *fainter* phases and also during *brighter* phases on luminosity suggest a constancy of the spectral index. This stability of the X-ray spectral shape over the *bright* and *faint* phases was also been confirmed by the WFC *BeppoSAX* measurements in the 2 – 28 keV band which showed minimal spectral changes (den Hartog et al. 2003).

The stability of the index was noted previously by FT11, for a number of NS LMXB at different luminosities. They collected X-ray spectra obtained by *BeppoSAX* and demonstrated the relative stability of spectral index  $\alpha$  approximately of 1 ( $\Gamma = \alpha + 1$ ) for quite a few NS sources X 1658-298, GX 354-0, GS 1826-238, 1E 1724-3045, Cyg X-1, Sco X-1, GX 17+2 and GX 349+2 at different spectral states. Recently ST11 presented results of analysis of X-ray spectra for *atoll* source 4U 1728-34, detected with *BeppoSAX* and *RTXE* at different

luminosities and values of the best-fit electron temperatures. These results indicate that the value of the index varies slightly about a value of 1, (or the photon index varies around 2) independently of the electron temperature of the Compton cloud  $kT_e$  and luminosity. This unique stability of the photon index may be an intrinsic property of NS at least for the *atoll* sources. It is probably determined by common physical conditions for this class of sources. FT11 & ST11 interpreted this quasi-stability of the index  $\Gamma$  in the framework of a model in which the spectrum is dominated by a strong thermal Comptonized component formed in the transition layer (TL) located between the accretion disk and neutron star surface. Indeed, the index quasi-stability takes place when the energy release in the TL is much higher than the photon energy flux coming from the accretion disk and illuminating the TL.

The evolution of spectral parameters of compact objects in X-ray binaries is of great interest for understanding their nature. It is well known that many black hole (BH) candidate binaries exhibit correlations between mass accretion rate  $\dot{M}$  and photon power-law index  $\Gamma$  [see Shaposhnikov & Titarchuk (2009) and Titarchuk & Seifina (2009), hereafter ST09 and TS09, respectively]. In the soft states of BHs these index- $\dot{M}$  correlations almost in any case show a saturation of  $\Gamma$  at high values of the  $\dot{M}$ . This saturation effect can be considered as a black hole signature or equivalently as a signature of a converging flow into BH (ST09 and TS09).

In this Paper we present the analysis of the *BeppoSAX* available observations and *RXTE*/PCA observations during 1996 – 2010 years for GX 3+1. In §2 we present the list of observations used in our data analysis while in §3 we provide the details of X-ray spectral analysis. We analyze an evolution of X-ray spectral and timing properties during the state transition in §4. We make our conclusions in §5.

## 2. Data Selection

Broad band energy spectra of the source were obtained combining data from three *BeppoSAX* Narrow Field Instruments (NFIs): the Low Energy Concentrator Spectrometer (LECS) for 0.3 – 4 keV (Parmar et al. 1997), the Medium Energy Concentrator Spectrometer (MECS) for 1.8 – 10 keV (Boella et al. 1997) and the Phoswich Detection System (PhDS) for 15 – 60 keV (Frontera et al. 1997). The SAXDAS data analysis package is used for processing data. For each of the instruments we performed the spectral analysis in the energy range for which response matrix is well determined. The LECS data have been re-normalized based on MECS. Relative normalization of the NFIs were treated as free parameters in model fitting, except for the MECS normalization that was fixed at a value of 1. We then checked this fitting procedure if these normalizations were in a standard range for

each instruments<sup>1</sup>. In addition, spectra are rebinned accordingly to energy resolution of the instruments in order to obtain significant data points. We rebinned the LECS spectra with a binning factor which is not constant over energy (Sect.3.1.6 of Cookbook for the *BeppoSAX* NFI spectral analysis) using template files in GRPPHA of XSPEC <sup>2</sup>. Also we rebinned the PhDS spectra with a linear binning factor of 2, grouping two bins together (resulting bin width is 1 keV). Systematic error of 1% have been applied to these analyzed spectra. In Table 1 we listed the *BeppoSAX* observations used in our analysis.

We have analyzed the available data obtained with *RXTE* (Bradt et al. 1993) which have been found in the time period from October 1996 to September 2010 [see also a review by Galloway et al. (2008)]. In our investigation we selected 101 observations made at different count rates (luminosity states) with a good coverage of rise-decay transition tracks. We have made an analysis of *RXTE* observations of GX 3+1 during fourteen years for 7 intervals indicated by blue rectangles in Figure 1 (*top*).

*RXTE*/PCA spectra have been extracted and analyzed, wherein PCA *Standard 2* mode data, collected in the 3 – 50 keV energy range, using the most recent release of PCA response calibration (ftool pcarmf v11.1). The relevant deadtime corrections to energy spectra have been applied. We used the data which are available through the GSFC public archive (<http://heasarc.gsfc.nasa.gov>). In Table 2 we presented the groups of *RXTE* observations which cover the source evolution from *faint* to *bright* (phase) events. Note that available *RXTE* data contains one “*bright* phase” set (*R4*) and six “*faint* phase” set (*R1 – R3, R5 – R7*). The PCA energy spectra were modeled using XSPEC astrophysical fitting software. Systematic error of 0.5% have been applied to the analyzed spectra.

We have also used public GX 3+1 data from the All-Sky Monitor (ASM) on-board *RXTE*, which show long-term quasi-periodic variability of the mean soft flux during  $\sim$  six years cycle (Fig. 1). We use definitions of the *fainter* and *brighter* on luminosity phases to relate these phases to the source luminosity and we demonstrate that during the bright/faint phase transition of GX 3+1 COMPTB normalization changes from 0.04 to 0.14  $L_{39}^{soft}/D_{10}^2$  where  $L_{39}^{soft}$  is the soft photon luminosity in units of  $10^{39}$  erg/s and  $D_{10}$  in units of 10 kpc is distance to the source.

---

<sup>1</sup><http://heasarc.nasa.gov/docs/sax/abc/saxabc/saxabc.html>

<sup>2</sup><http://heasarc.gsfc.nasa.gov/FTP/sax/cal/responses/grouping>

### 3. Spectral Analysis

In our spectral data analysis we use a model which consists a sum of a Comptonization component (*COMPTB*) [*COMPTB* is an XSPEC contributed model<sup>3</sup>, see Farinelli et al. (2008), hereafter F08], soft blackbody component of temperature  $T_{BB}$  and Gaussian line component. The *COMPTB* spectral component has the following parameters: temperature of the seed photons  $T_s$ , energy index of the Comptonization spectrum  $\alpha$  ( $= \Gamma - 1$ ), electron temperature  $T_e$ , illumination (Comptonization) fraction  $f$  of the Compton cloud by the soft (NS) photons,  $f = A/(1 + A)$ , and the normalization of the seed (NS) photon spectrum  $N_{COM}$ .

We include a simple *Gaussian* component in the model, which parameters are a centroid line energy  $E_{line}$ , the width of the line  $\sigma_{line}$  and the normalization  $N_{line}$  to fit the data in the 6 – 8 keV energy range. We also use the interstellar absorption with a column density  $N_H$ . It should be noted that we fixed certain parameters of the *COMPTB* component:  $\gamma = 3$  (low energy index of the seed photon spectrum) and  $\delta = 0$  because we neglect an efficiency of the bulk inflow effect vs the thermal Comptonization for NS GX 3+1. We apply a value of hydrogen column  $N_H = 1.6 \times 10^{22} \text{ cm}^{-2}$ , which was found by Oosterbroek et al. (2001).

Initially, we have tried a model consisting of an absorbed thermal component (*bbody*) and a thermal Comptonization component (*COMPTB*) but this model gave a poor description of data. Significant positive residuals around  $\sim 6.5$  keV suggest the presence of fluorescent iron emission line. The addition of *Gaussian* line component at 6.4 keV considerably improves fit quality and provides a statistically acceptable  $\chi_{red}^2$ .

At the first time the fluorescent iron emission line in GX 3+1 was detected by Oosterbroek et al. (2001) using *BeppoSAX* on 1999 August, 30 (id=20835001). Oosterbroek et al. (2001) successfully described this emission feature with the *Gaussian* line model and they used a model consisting of thermal component (dominating energy release around 1 keV) and a thermal Comptonization *tail* to describe the 0.1 – 50 keV continuum. However, they needed to add a 2% systematical uncertainty to LECS and MECS data to obtain acceptable  $\chi_{red}^2$ . We investigate a possibility to further improve a quality of the fit.

In Figure 2 we illustrate our spectral model as a basic model for fitting the *BeppoSAX* and *RXTE* spectral data for GX 3+1. We assume that accretion onto a neutron star takes place when the material passing through the two main regions: a geometrically thin accretion disk [the standard Shakura-Sunyaev disk, see Shakura & Sunyaev (1973)] and the transition layer (TL), where NS and disk soft photons are upscattered off hot electrons. In other words,

---

<sup>3</sup><http://heasarc.gsfc.nasa.gov/docs/software/lheasoft/xanadu/xspec/models/comptb.html>

in our picture, the emergent thermal Comptonization spectrum is formed in the TL, where thermal disk seed photons and soft photons from the neutron star are upscattered off the relatively hot plasma (electrons). Some fraction of these seed soft photons can be also seen directly. Red and blue photon trajectories shown in Fig. 2 correspond to soft (seed) and hard (up-scattered) photons respectively.

We show examples of X-ray spectra in Figs. 3 – 4 for *BeppoSAX* and *RXTE* data respectively. Spectral analysis of *BeppoSAX* and *RXTE* observations indicates that X-ray spectra of GX 3+1 can be described by a model with a Comptonization component represented by the *COMPTB* model. Moreover, for broad-band *BeppoSAX* observations this spectral model component is modified by photoelectric absorption at low energies.

On the *top* of Figure 3 we demonstrate the best-fit *BeppoSAX* spectrum of GX 3+1 in units of  $E * F(E)$  (*top*) [where  $F(E)$  is energy flux in erg, per keV and per second] using our model for *BeppoSAX* observation (id=20603001) carried out on 28 February – 1 March 1999. The data are presented by crosses and the best-fit spectral model  $wabs*(blackbody + COMPTB + Gaussian)$  by green line. The model components are shown by blue, red and crimson lines for *blackbody*, *COMPTB* and *Gaussian* components respectively. On the *bottom* we show  $\Delta\chi$  vs photon energy in keV. The best-fit model parameters are  $\Gamma=1.99\pm0.07$ ,  $kT_e=3.68\pm0.05$  keV and  $E_{line}=7.4\pm0.1$  keV (reduced  $\chi^2=1.08$  for 457 d.o.f) (see more details in Table 3). In particular, we find that an addition of the soft thermal component with temperature  $kT_{BB}=0.5-0.7$  keV to the model significantly improves the fit quality of the *BeppoSAX* spectra. For the *BeppoSAX* data (see Tables 1, 3) we find that the spectral index  $\alpha$  is of  $1.03\pm0.04$  (or the corresponding photon index  $\Gamma = \alpha + 1$  is  $2.03\pm0.04$ ).

Unfortunately *RXTE* detectors do not provide well calibrated spectra below 3 keV while the broad energy band of *BeppoSAX* telescopes allows us to determine the parameters of *blackbody* components at low energies. Thus, in order to fit the *RXTE* data we have to fix the temperature of *blackbody* component at a value of  $kT_{BB}=0.6$  keV obtained as an upper limit in our analyze of the *BeppoSAX* data. The best-fit spectral parameters using *RXTE* observations are presented in Table 4. In particular, we find that electron temperature  $kT_e$  of the *COMPTB* component varies from 2.3 to 4.5 keV, while the photon index  $\Gamma$  is almost constant ( $\Gamma = 1.99 \pm 0.02$ ) for all observations. It is worth noting that the width  $\sigma_{line}$  of *Gaussian* component does not vary significantly and it is in the range of 0.5 – 0.8 keV.

Color temperature  $kT_s$  of *COMPTB* component changes from 1.2 keV to 1.7 keV, which is consistent with that using the *BeppoSAX* data set of our analysis (see Table 3) and previous studies by Oosterbroek et al. (2001), den Hartog et al. (2003) and Chenevez et al. (2006). We should also emphasize that the temperature of the seed photons  $kT_s$  of the *COMPTB* component usually increases up to 1.7 keV in the fainter phases and generally decreases to



1.2 keV in the *bright* phases.

In Figure 4 we show an example of the best-fit *RXTE* spectrum of GX 3+1 for the fainter luminosity phases and the residuals (*bottom panel*) with  $\Delta\chi$  for the 94307-05-01-000 observation. Blue, red and purple lines stand for *blackbody*, *COMPTB* and *Gaussian* components, respectively.

In Figure 5 we also show examples of typical photon spectra  $E * F(E)$  spectral diagrams of GX 3+1 during the *fainter* phase (94307-05-01-00, *blue*) and the *brighter* phases (60022-01-13-01, *red*) detected with *RXTE* on MJD 55440.62 and 52544.48 respectively. The adopted spectral model shows a very good fidelity throughout all data sets used in our analysis. Namely, a value of reduced  $\chi_{red}^2 = \chi^2/N_{dof}$ , where  $N_{dof}$  is a number of degree of freedom, is less or about 1.0 for most observations. For a small fraction (less than 2%) of spectra with high counting statistics  $\chi_{red}^2$  reaches 1.5. However, it never exceeds our rejection limit of 1.7. Note that the energy range for the cases, in which we obtain the poor fit statistic (two among 101 spectra with  $\chi^2=1.7$  for 67 dof), are related to the iron line region. It is possible that the shape of iron line is more complex than a simple Gaussian (i.e. a blend of different energies, presence of the edge, or broadening by Comptonization). The fits tend to favor a broad line (see Table 4), which might be caused by Comptonization. However, this possible complexity is not well constrained by our data.

It is worth noting that we find some differences between our values of the best-fit model parameters and those in the literature. In particular, the photon index  $\Gamma$ , estimated by Oosterbroek et al. (2001) for observation id=20835001, is  $1.60 \pm 0.25$ . This discrepancy in index values can be a result of using slightly different spectral models by us and Oosterbroek et al. (2001).

Thus using the broad band *BeppoSAX* observations we can accurately determine all of the parameters of our spectral model while using the extensive observations of GX 3+1 by *RXTE* we are able to investigate the overall pattern of the source behavior during the spectral transitions in the 3 – 50 keV energy range.

## 4. Overall pattern of X-ray properties

### 4.1. Evolution of X-ray spectral properties during transitions

As was mentioned above, at time scales larger than one minute, GX 3+1 exhibits two kinds of variability, *slow* and *mild*. The former one (*slow*) has a time scale of order years. This *slow* variability are seen in the *faint* phases and *bright* phases which are related to

low and high luminosities, respectively. On the other hand the *mild* variability has a time scale of order of days and modulation depth in the 3 – 10 keV band is typically 20%. The ASM (2 – 12 keV) mean flux correlates with COMPTB normalization ( $N_{COM}$ ) and tends to anticorrelate with the electron plasma temperature of Compton cloud (CC)  $T_e$  (see Fig. 6). Such *mild* variability is detected for both the *fainter* and *brighter* phases for GX 3+1. It should be noted that the COMPTB normalization changes are larger in the *bright* phase than that during the *faint* phase, while the electron temperature  $T_e$  variations are almost the same for both phases.

One can relate *slow* and *mild* variabilities of GX 3+1 to slow and mild changes of mass accretion rate, respectively. The *slow* variability by factor 4 has been seen in the 1996 – 2010 observations by ASM/*RXTE*. The same kind of changes of the flux was also observed in the earlier observations by Makishima et al. (1983). In turn, in the next section it will be shown that the *slow* variability can be related to transitions between the *brighter* and *fainter* phases along with small variations of the electron temperature  $kT_e$ .

We found that the X-ray spectra of GX 3+1 over the *bright* and *faint* phases are quite stable. Moreover, we detected a constant 3 – 50 keV spectral shape over the *slow* and *mild* variability stages. The best-fit parameters are listed in Table 4. The *faint/bright phase* transitions are characterized by the spectra with an almost constant spectral index  $\alpha$  of 1, or photon index  $\Gamma$  of 2 (see Fig. 7). We have also established common characteristics of the rise-decay spectral transition of GX 3+1 based on their spectral parameter evolution of X-ray emission in the energy range from 3 to 50 keV using PCA/*RXTE* data. In Figures 4–5 we present typical examples of the *RXTE* bright and faint phase spectra for GX 3+1. In fact, one can clearly see from these Figures that the normalization of the thermal component is a factor of 2 higher in the *bright* phase than that in the faint phase, although the photon indices  $\Gamma$  for each of these spectra are concentrated around 2 (see Figs. 6 – 7).

In fact, we test the hypothesis of  $\Gamma_{appr} \approx 2$  using  $\chi^2$ -statistic criterion. We calculate the distribution of  $\chi_{red}^2(\Gamma_{appr}) = \frac{1}{N} \sum_{i=1}^N \left( \frac{\Gamma_i - \Gamma_{appr}}{\Delta\Gamma_i} \right)^2$  versus of  $\Gamma_{appr}$  and we find a sharp minimum of function  $\chi_{red}^2(\Gamma_{appr})$  around 1 which takes place in the range of  $\Gamma_{appr} = 1.99 \pm 0.01$  with a confidence level of 67% and  $\Gamma_{appr} = 1.99 \pm 0.02$  with a confidence level 99% for 101 d.o.f. (see the similar Figure of  $\chi_{red}^2(\Gamma_{appr})$  for 4U 1728-34 in ST11). Using *BeppoSAX* data FT11 suggested that the photon index  $\Gamma$  is approximately 2 for many NS binaries which are observed in different spectral states. FT11 characterize the spectral state by a value of electron temperature  $T_e$  and they show that  $\Gamma = 2 \pm 0.2$  (or  $\alpha = 1 \pm 0.2$ ) when  $kT_e$  changes from 2.5 to 25 keV.

A number of X-ray flaring episodes of GX 3+1 has been detected with *RXTE* during

2001–2002 (*R4* set) with a good rise-decay coverage. We have searched for common spectral and timing features which can be revealed during these spectral transition episodes. We present the combined results of the spectral analysis of these observations using our spectral model  $wabs * (blackbody + COMPTB + Gaussian)$  in Figures 6–7. ASM/*RXTE* count rate is shown on the top panel of these Figures. Further, from the top to the bottom, we show the model flux in two energy bands 3 – 10 keV (*blue points*) and 10 – 50 keV (*crimson points*). In the next panel we show a change of the TL electron temperature  $kT_e$ . One can clearly see the *low amplitude* spectral transition *on time scales of  $\sim 1 - 2$  days* from the *brighter* phase to the *faint* phase during the time period from MJD 52000 to MJD 52200 while  $kT_e$  only varies from 2.3 keV to 4.5 keV during this transition.

Normalizations of the *COMPTB* and *blackbody* component (*crimson* and *blue* points respectively) are shown in the next panel of Figs. 6 and 7. In particular, one can see from Figures 6–7 how the *COMPTB* normalization  $N_{COM}$  correlates with the variations of ASM count rate and the model flux in 3-10 keV energy band. On the other hand, the normalization of the *blackbody* component  $N_{BB}$  is almost constant except at the mild variability episode peak, when  $N_{BB}$  increases from 0.02 to 0.14 (see blue points in Figure 6 at MJD=52130 and 52170). Moreover these spectral variability transitions are related to a noticeable increase of flux in the 3 – 10 keV energy range and corresponding decrease of flux that takes place in the 10 – 50 keV energy range (see the second panels from above in Figs. 6 – 7).

The illumination fraction  $f$  varies from 0.1 to 0.9 as seen from Figure 8 while the index  $\alpha$  only slightly varies with time around 1 (or  $\Gamma \sim 2$ ) (see Figs. 6–7). However in most cases the soft disk radiation of GX 3+1 is subjected to reprocessing in a Compton cloud and only some fraction of the soft photon emission component ( $1 - f$ ) is directly seen by the Earth observer. Note that  $f$  changes with *COMPTB* normalization (see Fig. 8, the inner panel in the left-hand upper corner). The energy spectrum of GX 3+1 during almost all states is dominated by a Comptonized component while the direct soft photon emission is always weaker and detectable in the flaring episodes only (see also Figs. 6–7).

Note that for BHs a definition of spectral transition involves a change of photon index  $\Gamma$  (see e.g. ST09). However there is no one-to-one correspondence between  $\Gamma$  and cutoff (or efold) energy  $E_{fold}$ . Titarchuk & Shaposhnikov (2010) demonstrate using *RXTE* data for BH binary XTE J1550-564 that  $E_{fold}$  decreases when  $\Gamma$  increases from 1.4 to 2.1 – 2.2 until  $\Gamma$  reaches 2.2 and then  $E_{fold}$  increases. Thus *for a BH the main parameter used for the spectral transition definition is a variable photon index  $\Gamma$  which monotonically increases when the source goes into the bright phase*.

It is important to emphasize once again that in the NS binary GX 3+1 the transition from the *faint* phase to the *bright* phase takes place when *COMPTB* normalization  $N_{COM} =$

$L_{39}^{soft}/D_{10}^2$  changes from 0.04 to 0.15. Thus, we define the NS spectral transition in terms of the COMPTB normalization. In this case the faint phase is characterized by the low normalization value while the *bright* phase is related to the high normalization value. In Figure 9 we demonstrate the dependence of COMPTB normalization  $L_{39}^{soft}/D_{10}^2$  on  $kT_e$  using these best-fit parameters for GX 3+1 and 4U 1728-34 for the *BeppoSAX* and *RXTE* data. From this Figure one can clearly see a monotonic behavior  $N_{COM}$  vs  $kT_e$ , namely  $kT_e$  decreases when the soft flux increases. It is worth noting that the  $kT_e$  values obtained using GX 3+1 data for *BeppoSAX* and *RXTE* reach the asymptotic value of about 2.5 keV at high values of the soft flux ( $N_{COM} > 0.05$ ).

To demonstrate transition properties of GX 3+1 in terms of flux (or luminosity) we define the hard color (HC) as a ratio of the flux in the 10 – 50 keV to that in the 3 – 50 keV energy band, and the soft color (SC) as a ratio of the flux in the 3 – 10 keV to that in the 10 – 50 keV energy range. Plotting HC versus SC we created *our color – color* diagram (CD, see the left panel of Fig. 10 ) for two atoll sources GX 3+1 (*pink*) and 4U 1728-34 (*blue*). As it appears from this Figure the tracks of these two sources display a smooth and continuous (monotonic) function, pointing out the similar physical mechanism of hard/soft flux transition during a long-term source evolution for these two objects. In Fig. 10 (*right* panel) we demonstrate a fragment of ASM light curve of GX 3+1 which illustrates two types of flux variability. The long-term time trend (from bright to faint) is related to COMPTB normalization changes and while the second one shows short-term time variations (UB-LB) related to the Compton cloud electron temperature variations. The blue line displays a mean count rate and indicates to long-term variability of GX 3+1 flux. Note that the track of Fig. 10 (*left* panel) reflects a long-term evolution of GX 3+1.

It is worth noting that among all NSs only a few of *atoll* and Z-sources demonstrate a full track on CD in a wide range of luminosity. For example, *atoll* sources, such as 4U 1728-34, usually show a wide range of spectral states during transitions which are related to changes of the total luminosity and mass accretion rate. One can establish a substantial difference between a NS and a BH due to these flare episodes when a source evolves from the *faint* phase to the *bright* phase and when the plasma temperature of a Comptonized region changes remarkably (like in 4U 1728-34 from 2.5 keV to 15 keV during IS – B states). On the other hand GX 3+1 shows significant changes in the total luminosity but with only a slight variation of electron temperature  $kT_e$  in its *banana* state. However, the photon index  $\Gamma$  stays around a value of 2 and is independent of the soft photon luminosity both in the faint phase and the bright phase.

## 4.2. Timing properties during LB-UB transitions

The *RXTE* light curves have been analyzed using the *powspec* task from FTOOLS 5.1. The timing analysis PCA/*RXTE* data was performed in 13 – 30 keV energy range using the *event* mode. The time resolution for this mode is  $1.2 \times 10^{-4}$  s. We generated power density spectra (PDS) in 0.1 – 500 Hz frequency range using light curves with  $10^{-3}$ -second time resolution. We subtracted the contribution due to Poissonian noise and Very Large Event Window for all PDSs. We used QDP/PLT plotting package to model PDS.

Previously, timing analysis of PCA/*RXTE* data for GX 3+1 observed on August 1999 (our R3 set), when the sources was in *lower banana* phase, was made by Oosterbroek et al. (2001). We investigated a timing behavior of GX 3+1 for our data set during all transitions between *lower banana* and *upper banana* phases (see Fig. 11). In particular, the power spectrum of GX 3+1 consists of very low-frequency noise (VLFN, described by a power-law) and high-frequency noise [HFN, described by a cutoff-power-law, see van der Klis (2005)].

In the LB phases (A *red*, 60022-01-13-01, MJD=52554; A *blue*, 60022-01-01-00, MJD=51998) the best-fit to the average power spectrum results in rms VLFN-component of 2% (in the 0.1 – 1 Hz range) described by power-law  $\nu^{-\alpha_{LF}}$  with the index of  $\alpha_{LF} \sim 1.7$ , whereas HFN rms (in the 1 – 100 Hz range) has 4.7% with  $\alpha_{HF} \sim 1.0$  and  $\nu_{cutoff} \sim 30$  Hz. Generally the index of VLFN  $\alpha_{LF}$  gradually decreases from 1.7 to 1.4 toward to UB. However in the vicinity of a transition point between LB and UB (red histogram of panel B of Fig. 11)  $\alpha_{LF}$  jumps to 1.8 (B *red*, 94307-05-01-00, MJD=55129) and decreases again to 1.4 (B *blue*, 60022-01-11-03, MJD=52357). In general, the UB power spectra of GX 3+1 are dominated by the VLFN with the brake at around 20 Hz at the lowest  $kT_e = 2.4$  keV (see *blue* B point on the right-hand panel of Fig. 11). Specifically, during UB (*blue* histogram of panels B of Fig. 11) one can see strong VLFN (rms= $5.1 \pm 0.4\%$ ,  $\alpha_{LF}=1.4 \pm 0.3$ ,  $\chi^2=139$  for 102 d.o.f; all parameter errors correspond to  $1\sigma$  confidence level) and HFN with rms= $1.7 \pm 0.3\%$  and break frequency shifted from 30 Hz to 6 Hz. After UB GX 3+1 again returns to the LB showing similar to panel A properties of power density spectra (see panel C of Fig. 11).

Note that these components and their CD evolution are typical for of atoll-sources in the banana state (Hasinger & van der Klis 1989) and caused by mass accretion rate change (van der Klis 2005). This phase identification is supported by a combination of spectral (see Sect. 4.1) and timing properties in an agreement with *atoll-Z* scheme.

While the aforementioned CD evolution of power spectra of GX 3+1 occurs on time scales from hours to days, we detected similar patterns for power spectrum evolution during LB – UB transitions for both *faint phase* and *bright phase* on luminosity during long-term variability within 14 years with a quasi-periodic trend during six years. The similarity of

LB – UB transitions which are independent of bright/faint phases on luminosity indicates to similar accretion configurations in all phases.

In a previous analysis of other RXTE data of GX 3+1 Oosterbroek et al. (2001) report VLFN and HFN values, in LB state, which are similar to our values in interval R3, with the exception of VLFN strength for which they report 7.5% rms while we find 1.7% rms. All of the VLFN and HFN values of the analysis of EXOSAT data reported by Hasinger & van der Klis (1989) for GX 3+1 agree with our results.

### 4.3. Comparison of spectral and timing characteristics *atoll* sources GX 3+1 and 4U 1728-34

#### 4.3.1. Quasi-Constancy of the photon index

The *atoll* sources GX 3+1 and 4U 1728-34 demonstrate a similar behavior of the parameter  $\Gamma$  vs mass accretion rate (or our COMPTB normalization), namely the quasi-constancy of the photon index  $\Gamma \approx 2$  and almost identical long-term variations of ASM mean count rate (see also ST11). According to FT11 and ST11 this observational fact can presumably indicate that the energy release in the transition layer for these two sources is much higher than cooling flux of the soft (disk) photons.

#### 4.3.2. A difference of the electron temperature $kT_e$ ranges in GX 3+1 and 4U 1728-34

A comparison of the best-fit spectral parameters for these two *atoll* sources shows that a *slow* variability is generally related to changes of COMPTB normalization, and a *mild* variability is mainly correlated with the electron temperature variations (see Fig 10). Note that the ranges of disk and NS temperatures are similar for both of these objects, namely  $kT_{BB} \simeq 0.6$  keV and  $kT_s = 1.2 - 1.7$  keV respectively. On the other hand variations of the electron temperature  $kT_e$  are quite different. The electron temperature  $kT_e$  changes in a wide range  $kT_e = 2.5 - 15$  keV for 4U 1728-34, while for GX 3+1  $kT_e$  varies in a narrow range from 2.3 to 4.5 keV (see Figs. 8 – 9). The reason for this difference of temperature ranges is quite obvious. While 4U 1728-34 shows an evolution from the extreme island state (EIS) to the upper banana state (UB) [see, Di Salvo et al. (2001) and ST11] GX 3+1 demonstrates only a short LB – UB track on CD (see Fig. 8). These ranges of CD states are related to the ranges of  $kT_e$ .

### 4.3.3. Comparison of spectral evolution as a function of the COMPTB normalization for GX 3+1 and 4U 1728-34

We can also compare spectral parameter evolution for GX 3+1 and 4U 1728-34 using COMPTB normalization because the distances to these sources are almost the same (see Table 5). Namely, for GX 3+1 the distance is in the range of 4.2–6.4 kpc (Kuulkers & van der Klis 2000), whereas for 4U 1728-34 it is 4.5 kpc (van Paradijs 1978). In Figure 9 we show a correlation of COMPTB normalization presumably proportional to mass accretion rate) and the electron temperature  $kT_e$  for these two *atoll* sources. GX 3+1 demonstrates a wider range of COMPTB normalization (by factor of 2 higher than that for 4U 1728-34) while  $kT_e$  varies only from 2.5 to 4.5 keV. The common interval of  $kT_e$  for GX 3+1 and 4U 1728-34 is in the range 2.5 – 4.5 keV only and the low limit of the electron temperature of 2.5 keV takes place at the peak luminosity for 4U 1728-34 (see ST11) and during increases in luminosity for GX 3+1, i.e. during so called UB state (see Fig. 8).

### 4.3.4. Correlation of illumination parameter $f$ vs electron temperature $kT_e$ and its relation with different states on color-color diagram

One can see from Table 5 that the range of illumination fraction of Compton cloud (TL)  $f$  is wider for GX 3+1 (0.1 – 0.9) than that for 4U 1728-34 (0.5 – 1). It can be related to different illumination of the transition layer (TL) for these two sources. For 4U 1728-34 the solid angle viewed from NS changes by factor 2 whereas in GX 3+1 that changes by factor 4. However, the photon index  $\Gamma \approx 2$  for these two sources which indicates that the energy release in the transition layer for these two sources is much higher than cooling flux of the disk photons (see FT11 and ST11 for details of X-ray spectral formation in TL).

In Figure 8 we present a plot  $kT_e$  versus  $f = A/(1 + A)$  for *atoll* sources GX 3+1 and 4U 1728-34 during *mild* variability. *Pink/bright blue* and *blue/green* points correspond to *RXTE/BeppoSAX* observations of GX 3+1 and 4U 1728-34 respectively. COMPTB normalization measured in  $L_{39}^{soft}/D_{10}^2$  units versus  $f$  is plotted in the incorporated top left panel for long-term (*slow*) variability of GX 3+1 (see Table 4 for details). The bended arrows along the corresponding tracks correspond to an increase in mass accretion rate. On the right-hand side of Figure we also present the sequence of CD states which are listed according to the standard *atoll-Z* scheme (Hasinger & van der Klis 1989). Here we also show that the CD sequence is definitely related to the electron temperature  $kT_e$ . The diagram of  $T_e$  versus  $f$  demonstrates a clear correlation  $T_e$  and  $f$  while the diagram  $N_{COM}$  versus  $f$ , presented in the incorporated panel of Fig. 8 shows only chaotic scattering of points in a wide range of  $f \sim 0.2 - 0.9$ .

Moreover, we find two different track shapes on diagram of  $T_e$  versus  $f$  for two atoll sources GX 3+1 and 4U 1728-34 and their relations with the standard sequence of CD states (Fig. 8). When the fraction  $f$  increases, the electron temperature  $T_e$  decreases monotonically from approximately 4.5 keV to  $\sim 2.3$  keV for GX 3+1, while 4U 1728-34 demonstrates more complicated behavior pattern. At EIS, with a decrease of  $T_e$ , the fraction  $f$  slightly varies from 0.9 to 1. When  $T_e$  further decreases from 12 keV to 4 keV,  $f$  decreases from 0.9 to 0.5. Finally, during the LB-UB state transition  $f$  increases from 0.5 to 1.

Thus we show that the evolution CD states can be traced by the correlation between  $T_e$  and  $f$  too. Note that the tracks of  $f - T_e$  on this diagram resemble the atoll tracks on the standard color-color diagram (Schultz et al. 1989).

## 5. Conclusions

We present our analysis of the spectral properties observed in X-rays from the neutron star X-ray binary GX 3+1 during long-term transitions between the *faint* phase and the *bright* phase superimposed by short-term transitions between *lower banana* and *upper banana* states. We analyze all transition episodes for this source observed with *BeppoSAX* and *RXTE*. For our analysis we apply the good spectral coverage and resolution of *BeppoSAX* detectors from 0.1 to 200 keV along with *extensive RXTE* coverage in the energy range from 3 to 50 keV.

We show that the X-ray broad-band energy spectra during all spectral states can be adequately fitted by the combination of a *Blackbody*, a Comptonized and a *Gaussian* components. We also show that photon index  $\Gamma$  of the best-fit Comptonized component in GX 3+1 is almost constant, with a value of 2 and consequently is almost independent of *COMPTB* normalization  $L_{39}^{soft}/D_{10}^2$  which is presumably proportional to mass accretion rate  $\dot{m}$  (see Figs. 6 – 7, 11). We should remind a reader that this index stability has recently been suggested using X-ray observations of quite a few of other NS sources. Namely atoll sources: X 1658-298, GS 1826-238, 1E 1724-3045 and also Z-sources: Cyg X-2, Sco X-1, GX 17+2, GX 340+0, GX 349+2 were observed by *BeppoSAX* at different spectral states and also atoll source 4U 1728-34 observed by *BeppoSAX* and *RXTE* [see details in FT11 and ST11 respectively].

A wide variation of parameter  $f = 0.1 - 0.9$ , obtained in the framework of our spectral model, points out a significant variation of the illumination of Comptonization region (transition layer) by X-ray soft photons in GX 3+1.

Using *BeppoSAX* observations we find that there are two sources of blackbody emission,



one is presumably related to the accretion disk and another one is related to the NS surface for which temperatures of soft photons are about 0.7 keV and 1.3 keV, respectively.

We demonstrate that our analysis of X-ray spectral and timing properties in atoll source GX 3+1 allows us to distinguish between *mild* and long-term variabilities, and link them with LB – UB state transitions and transitions between *bright* and *faint* phases in luminosity, respectively. In this way we described *mild* flux variability between LB and UB states on time scale of hours – days in terms of two basic spectral parameters, the electron temperature  $kT_e$  and illumination fraction  $f$ . We argue that  $kT_e$  monotonically increases from 2.3 keV to 4.5 keV when GX 3+1 makes a transition from UB state to LB state. We also find, two noise components (VLFN & HFN) and their evolution during LB – UB transitions: the X-ray power spectra (PDS) in UB are dominated by very low frequency noise (VLFN) with the break around 20 Hz, whereas in LB the PDSs are dominated by a high frequency noise (HFN) in 1 – 100 Hz range and accompanied by reduced VLFN below  $\sim 1$  Hz.

We demonstrate that the photon index  $\Gamma \sim 2$  is approximately constant when the source moves from the faint phase to the bright phase and as well as during local transitions from *lower banana* to *upper banana*. In ST11 we presented strong theoretical arguments that the dominance of the energy release in the transition layer (TL) with respect to the soft flux coming from the accretion disk,  $Q_{disk}/Q_{cor} \ll 1$  leads to almost constant photon index  $\Gamma \approx 2$ .

Thus we argue that *the stability of this index is an intrinsic signature of atoll sources while in BHs the index monotonically changes with mass accretion rate and ultimately saturates* (see ST09 and ST11). Photon indices of BH candidates (GRS 1915+105, GX 339-4, SS 433, H1743-322, 4U 1543-47, Cyg X-1, XTE J1550-564 and GRO J1655-40) show clear correlation with mass accretion rate  $\dot{m}$  [ST09, TS09 and Seifina & Titarchuk (2010)]. This correlation is accompanied by an index saturation when  $\dot{m}$  exceeds a certain level. The behaviors of the index for GX 3+1 and 4U 1728-34 are clearly different from that for the sample of BHC sources. The photon index  $\Gamma \approx 2$  while mass accretion rate changes by factor 4.

We acknowledge discussion and editing of the paper content with Chris Shrader. We are very grateful to the referee whose constructive suggestions help us to improve the paper quality.

## REFERENCES

Asai, K., et al., 1993, PASPJ, 45, 801

- Boella, G. et al. 1997, *A&AS*, 122, 327
- Bowyer, S., Byram, E. T., Chubb, T. A., Friedman, H. 1965, *Science*, 147, Issue 3656, 394
- Bradt, H. V., Rothschild, R. E. & Swank, J. H. 1993, *A&AS*, 97, 355
- Chenevez, J. et al. 2006, *A&A*, 449, L5
- Christian, D. J. & Swank, J. H. 1997, *ApJS*, 109, 177
- den Hartog, P. R., et al. 2003, *A&A*, 400, 663
- Di Salvo, T., Mendez, M., van der Klis, M., Ford, E. & Robba, N.R. 2001 *ApJ*, 546, 1107
- Farinelli, R., Titarchuk, L., Paizis, A. & Frontera, F. 2008, *ApJ*, 680, 602 (F08)
- Farinelli, R. & Titarchuk, L., 2011, *A&A*, 525, 102 (FT11)
- Ford, E. C., van der Klis, M., Mendez, M., et al. 2000, *ApJ*, 537, 368
- Frontera, F. et al. 1997, *SPIE*, 3114, 206
- Galloway, D.K. et al. 2008, *ApJS*, 179, 360
- Hasinger, G. & van der Klis, M. 1989, *A&A*, 225, 79
- Homan, J., van der Klis, M., Wijnands, R., Vaughan, B., & Kuulkers, E. 1998, *ApJ*, 499, L41
- Hanson, C.J. & van Horn, H. M. 1975, *ApJ*, 195, 735
- Kuulkers, E. 2002, *A&A*, 383, L5
- Kuulkers, E & van der Klis, M. 2000, *A&A*, 356, L45
- Lewin, W. H. G., van Paradijs, J., Hasinger, G., et al. 1987, *MNRAS*, 226, 383
- Makishima, K. et al. 1983, *ApJ*, 267, 310
- Molkov, S. V., Grebenev, S. A., Pavlinskij, M. N. & Sunyaev, R. A., 1999, Proc. of the 3rd INTEGRAL Workshop “The Extreme Universe”, *ApLc*, 38, 141
- Muno, M. P., Remillard, R. A., & Chakrabarty, D. 2002, *ApJ*, 568, L35
- Naylor, T., Charles, P.A. & Longmore, A.J. 1991, *MNRAS*, 252, 203
- Oosterbroek, T., Barret, D., Gianazzi, M. & Ford, E.C. 2001, *A&A*, 366, 138

- Paizis, A., Farinelli, R., Titarchuk, L., et al. 2006, *A&A*, 459, 187
- Pavlinisky, M. N., Grebenev, S. A. & Sunyaev, R. A. 1994, *ApJ*, 425, 110
- Parmar, A. N., et al. 1997, *A&AS*, 122, 309
- Schnerr, R. S., Reerink, T., van der Klis, M., et al. 2003, *A&A*, 406, 221
- Schultz, N. S., Hasinger, G. & Trumper, J. 1989, *A&A*, 225, 48
- Seifina, E. & Titarchuk, L. 2011, *ApJ*, 737, 128 (ST11)
- Seifina, E. & Titarchuk, L. 2010, *ApJ*, 722, 586 (ST10)
- Shakura, N. I., & Sunyaev, R. A. 1973, *A&A*, 24, 337
- Shaposhnikov, N. & Titarchuk, L. 2009, *ApJ*, 699, 443 (ST09)
- Stella, L., White, N. E., & Taylor, B. G. 1985, in *Recent Results on Cataclysmic Variables*, 125-128
- Strohmayer, T. 1998, in *American Institute of Physics Conference Series*, 397 (astro-ph/9802022v1)
- Titarchuk, L. & Shaposhnikov, N. 2010, *ApJ*, 724, 1147
- Titarchuk, L. & Seifina, E. 2009, *ApJ*, 706, 1463
- Titarchuk, L. G. & Osherovich, V. A. 1999, *ApJ*, 518, L95
- van der Klis, M. 2005, *Ap&SS*, 300, 149
- van der Klis, M. 2000, *ARA&A*, 38, 717
- van Paradijs, J. 1978, *Nature*, 274, 650
- Woosley, S. E. & Taam, R. E. 1976, *Nature*, 263, 101
- Wijnands, R., van der Klis, M., & van Paradijs, J. 1998, in *IAU Symp. 188: The Hot Universe*, 370

Table 1. The list of *BeppoSAX* observations of GX 3+1 used in our analysis.

Obs. ID	Start time (UT)	End time (UT)	MJD interval	CD state
20603001	1999 Feb. 28 11:02:15	1999 Feb. 30 09:14:15	51237.4-51238.9	<i>upper banana</i>
20835001	1999 Aug. 30 18:33:08	1999 Aug. 31 04:54:32	51420.8-51421.9 <sup>1</sup>	<i>lower banana</i>

Reference. (1) Oosterbroek et al. (2001)

Table 2. The list of *RXTE* observation groups of GX 3+1

Number of set	Dates, MJD	RXTE Proposal ID	Dates UT	Rem.	Phase on lumonosity
R1	50365	10069	Oct. 9 03:36:00 – 04:08:00, 1996		<i>faint</i>
R2	50962-51118	30042, 30048	May 29 – Nov. 1, 1998		<i>faint</i>
R3	51324-51445	40023, 40425 <sup>1</sup>	May 26 – Sept. 24, 1999	<i>BeppoSAX</i>	<i>faint</i>
R4	51998-52554	60022	March 30, 2001 – Oct. 7, 2002		<i>bright</i>
R5	52881	80105	Aug. 30 03:53:36 – 06:29:13, 2003		<i>faint</i>
R6	53108-53280	90022	Apr. 13 – Oct. 2, 2004		<i>faint</i>
R7	55440.6-55440.8	94307	Sept. 1 15:00:32 – 21:07:58, 2010		<i>faint</i>

References: (1) Oosterbroek et al. (2001)

Table 3. Best-fit parameters of spectral analysis of *BeppoSAX* observations of GX 3+1 in 0.3-50 keV energy range<sup>†</sup>.  
Parameter errors correspond to  $1\sigma$  confidence level.

Observational ID	MJD, day	$T_{BB}$ keV	$N_{BB}^{\dagger\dagger}$	$T_s$ keV	$\alpha =$ $\Gamma - 1$	$T_e,$ keV	$\log(A)$	$N_{COM}^{\dagger\dagger}$	$E_{line},$ keV	$N_{line}^{\dagger\dagger}$	$\chi_{red}^2$ (d.o.f.)
20603001	51237.5	0.47(3)	2.65(2)	1.30(3)	0.99(7)	3.68(5)	0.09(4)	4.18(3)	7.4(1)	0.55(4)	1.08(457)
20835001	51420.8	0.62(5)	1.61(1)	1.21(5)	1.07(4)	2.4(2)	-0.32(8)	3.56(2)	6.0(1)	0.43(4)	1.16(445)

<sup>†</sup> The spectral model is  $wabs * (blackbody + COMPTB + Gaussian)$ , normalization parameters of *blackbody* and *COMPTB* components are in units of  $L_{37}^{soft}/d_{10}^2$  where  $L_{37}^{soft}$  is the soft photon luminosity in units of  $10^{37}$  erg/s,  $d_{10}$  is the distance to the source in units of 10 kpc and *Gaussian* component is in units of  $10^{-2} \times total \ photons \ cm^{-2} s^{-1}$  in line. <sup>††</sup> Gaussian component is in units of  $10^{-2} \times total \ photons \ cm^{-2} s^{-1}$  in line.

Table 4. The best-fit parameters of spectral analysis of PCA/*RXTE* observations of GX 3+1 in 3-50 keV energy range<sup>†</sup>. Parameter errors correspond to 1 $\sigma$  confidence level.

Observational ID	MJD, day	$\alpha = \Gamma - 1$	$T_e$ , keV	log(A)	$N_{COM}^{\dagger\dagger}$	$T_s$ , keV	$N_{Bbody}^{\dagger\dagger}$	$E_{line}$ , keV	$\sigma_{line}$ , keV	$N_{line}^{\dagger\dagger}$	$\chi_{red}^2$ (d.o.f.)	$F_1/F_2^{\dagger\dagger}$
10069-03-01-00	50365.172	1.00(8)	2.40(2)	0.03(1)	10.88(2)	1.10(8)	2.74(5)	6.53(3)	0.58(5)	0.95(4)	1.1(67)	6.79/1.28
30042-04-01-00	50962.598	1.0(1)	2.52(1)	-0.04(3)	6.3(1)	1.65(5)	3.17(3)	6.51(2)	0.5(1)	0.46(2)	1.50(67)	4.13/0.80
30042-04-02-00	50973.668	1.02(7)	2.42(1)	-0.1(1)	9.9(1)	1.17(4)	2.6(1)	6.5(1)	0.5(1)	0.37(8)	1.12(67)	2.69/1.49
30048-01-01-00	51011.138	0.99(2)	2.44(2)	0.18(8)	6.3(2)	1.45(8)	3.12(8)	6.42(8)	0.6(1)	0.7(1)	0.82(67)	4.68/1.03
30042-04-03-00	51113.941	1.01(2)	3.15(2)	0.39(5)	4.00(6)	1.5(1)	3.05(2)	6.53(1)	0.50(8)	0.42(1)	0.87(67)	3.26/1.31
30042-04-03-01	51114.207	1.03(3)	3.17(2)	0.41(5)	4.07(6)	1.5(1)	3.07(2)	6.58(1)	0.52(7)	0.44(1)	0.91(67)	3.62/1.56
30042-04-04-00	51118.739	1.1(1)	3.52(8)	0.45(6)	3.7(1)	1.7(5)	2.86(3)	6.51(4)	0.6(2)	0.47(2)	1.18(67)	3.03/1.34
40023-01-01-00	51324.737	1.0(3)	2.48(2)	0.02(1)	5.98(8)	1.6(2)	2.62(8)	6.43(9)	0.67(9)	0.9(1)	1.35(67)	4.68/1.03
40023-01-01-01	51325.310	1.0(2)	2.40(1)	0.23(3)	5.78(6)	1.6(2)	2.64(9)	6.43(5)	0.67(8)	0.73(7)	0.75(67)	4.15/0.88
40023-01-01-02	51325.542	1.(1)	2.46(1)	-0.01(1)	5.85(4)	1.6(2)	2.38(8)	6.45(5)	0.62(6)	0.73(8)	1.26(67)	4.06/0.77
40023-01-03-00	51390.248	1.0(1)	2.54(1)	0.01(1)	6.20(6)	1.56(8)	2.6(1)	6.49(7)	0.60(7)	0.7(1)	0.94(67)	4.33/0.88
40023-01-02-00	51398.243	0.9(2)	2.53(1)	0.04(2)	5.61(5)	1.4(1)	2.68(9)	6.45(5)	0.64(6)	0.76(9)	1.01(67)	3.99/0.81
40023-01-02-01	51398.188	0.9(1)	2.50(2)	0.02(2)	5.50(5)	1.5(1)	2.78(7)	6.45(5)	0.48(8)	0.61(9)	1.01(67)	3.93/0.76
40023-01-02-02	51399.644	0.9(1)	2.49(8)	0.01(1)	6.93(8)	1.2(1)	2.47(5)	6.46(9)	0.69(9)	0.96(8)	0.53(67)	4.74/0.94
40023-01-02-03	51400.131	1.01(6)	2.51(5)	0.06(2)	6.19(7)	1.2(1)	3.16(4)	6.38(5)	0.8(1)	1.09(6)	0.71(67)	4.34/0.86
40023-01-02-04	51400.192	1.01(9)	2.4(1)	0.06(2)	5.77(6)	1.18(3)	2.83(5)	6.45(9)	0.52(5)	0.61(6)	0.85(67)	3.97/0.75
40023-01-02-05	51400.259	1.0(1)	2.6(1)	-0.09(5)	6.72(6)	1.25(2)	2.9(1)	6.50(7)	0.46(7)	0.63(9)	0.77(67)	4.64/0.93
40023-01-02-06	51400.325	1.0(1)	2.45(7)	0.18(9)	6.19(5)	1.25(8)	3.04(8)	6.46(8)	0.41(6)	0.45(9)	0.92(67)	4.26/0.92
40023-01-02-07	51400.723	1.0(1)	2.45(1)	0.11(2)	6.85(4)	1.20(8)	2.38(7)	6.45(8)	0.47(5)	0.45(8)	0.92(67)	4.70/0.98
40023-01-04-00	51404.304	0.99(1)	4.50(4)	-0.9(1)	3.99(9)	1.82(3)	3.63(9)	4.55(5)	0.50(7)	0.70(6)	1.70(67)	4.16/0.94
40023-01-03-01	51405.307	1.(1)	2.48(1)	0.09(2)	6.38(6)	1.20(8)	2.32(9)	6.55(8)	0.56(9)	0.60(8)	1.28(67)	4.39/0.92
40425-01-01-00	51420.779	1.0(1)	3.05(7)	-0.5(5)	6.05(8)	1.59(8)	4.01(6)	6.5(1)	0.6(1)	1.05(4)	0.82(67)	4.84/0.97
40425-01-01-01	51420.846	1.09(5)	2.83(9)	-0.31(7)	6.85(7)	1.59(9)	4.09(9)	6.5(1)	0.62(9)	0.87(9)	1.05(67)	5.36/1.21
40425-01-01-02	51421.018	1.05(1)	2.8(1)	-0.29(3)	6.23(2)	1.59(5)	3.74(9)	6.5(1)	0.61(8)	0.85(2)	1.34(67)	4.88/1.10
40425-01-01-03	51421.084	1.01(1)	3.29(9)	-0.29(3)	5.83(5)	1.59(8)	4.19(6)	6.5(1)	0.65(5)	0.86(3)	1.30(67)	4.87/0.98
40425-01-01-04	51421.151	1.0(1)	2.85(8)	-0.33(6)	4.77(4)	1.55(7)	3.91(3)	6.38(2)	0.58(7)	0.99(2)	1.15(67)	4.87/0.98
40425-01-01-05	51421.218	1.08(9)	2.99(5)	-0.43(3)	5.22(5)	1.49(8)	4.11(2)	6.38(4)	0.59(4)	1.11(8)	1.39(67)	4.47/0.88

Table 4—Continued

Observational ID	MJD, day	$\alpha =$ $\Gamma - 1$	$T_e,$ keV	$\log(A)$	$N_{COM}^{\dagger\dagger}$	$T_s,$ keV	$N_{Bbody}^{\dagger\dagger}$	$E_{line},$ keV	$\sigma_{line},$ keV	$N_{line}^{\dagger\dagger}$	$\chi_{red}^2$ (d.o.f.)	$F_1/F_2^{\dagger\dagger\dagger}$
40425-01-01-06	51421.285	1.02(8)	2.69(6)	-0.19(6)	4.24(2)	1.35(7)	3.79(3)	6.38(3)	0.62(8)	0.87(6)	1.36(67)	3.77/0.74
40023-01-05-00	51445.320	0.99(3)	2.59(9)	-0.06(4)	7.38(7)	1.24(8)	2.7(1)	6.47(8)	0.46(4)	0.62(4)	0.84(67)	4.96/1.03
40023-01-03-01	51445.599	1.0(1)	2.35(4)	0.73(9)	6.44(7)	1.16(7)	2.32(1)	6.54(9)	0.4(1)	0.52(8)	1.70(67)	4.80/1.13
60022-01-01-00	51998.64	1.06(3)	2.49(1)	0.04(1)	12.03(1)	1.20(5)	2.86(2)	6.24(2)	0.5(1)	1.50(6)	1.07(67)	7.94/1.69
60022-01-01-01	51998.71	1.03(9)	2.52(2)	0.07(4)	12.97(3)	1.20(7)	2.31(3)	6.5(1)	0.56(8)	1.33(5)	1.09(67)	8.43/1.91
60022-01-01-02	51998.78	1.01(3)	2.57(1)	-0.04(1)	11.92(3)	1.2(1)	3.26(2)	6.59(5)	0.58(7)	1.33(7)	0.87(67)	8.43/1.91
60022-01-01-03	51999.78	1.02(7)	2.47(3)	0.04(1)	12.31(4)	1.20(3)	2.39(4)	6.55(4)	0.55(7)	1.57(6)	1.15(67)	8.02/1.69
60022-01-02-00	52028.61	1.00(9)	2.51(6)	0.03(1)	11.50(3)	1.20(5)	2.74(4)	6.56(2)	0.53(6)	1.22(5)	1.13(67)	7.56/1.62
60022-01-02-01	52028.94	1.01(3)	2.54(2)	0.01(1)	11.73(2)	1.20(6)	2.51(6)	6.50(6)	0.59(5)	1.23(3)	1.05(67)	7.62/1.65
60022-01-01-04	52029.47	1.07(3)	2.52(1)	0.06(2)	13.88(6)	1.17(9)	3.15(2)	6.50(7)	0.62(7)	1.61(8)	0.98(67)	9.15/2.02
60022-01-01-05	52029.61	1.03(6)	2.51(2)	0.2(1)	13.36(3)	1.20(5)	2.39(6)	6.51(6)	0.50(8)	1.03(5)	0.88(67)	8.80/2.21
60022-01-01-06	52029.69	1.05(3)	2.53(4)	-0.01(1)	11.54(4)	1.20(4)	2.84(9)	6.54(2)	0.53(9)	1.26(6)	1.40(67)	7.57/1.58
60022-01-03-00	52067.39	1.01(4)	2.53(1)	0.21(7)	13.35(3)	1.20(7)	2.62(4)	6.51(2)	0.5(1)	1.22(3)	1.09(67)	8.87/2.22
60022-01-03-01	52067.58	1.03(5)	2.52(3)	0.04(1)	12.65(3)	1.20(4)	2.36(5)	6.55(8)	0.35(4)	1.28(3)	1.30(67)	8.22/1.82
60022-01-03-01	52068.30	1.07(9)	3.16(2)	-0.46(9)	10.82(4)	1.20(5)	5.41(3)	6.36(3)	0.41(8)	1.58(4)	1.20(67)	8.24/1.94
60022-01-04-03	52102.363	1.03(9)	3.25(9)	-0.57(8)	9.44(7)	1.31(7)	5.47(4)	7.07(3)	0.50(9)	1.64(5)	1.07(67)	7.44/1.60
60022-01-04-00	52103.361	1.01(5)	2.72(5)	-0.20(8)	9.7(1)	1.30(6)	6.65(9)	7.09(4)	0.52(9)	1.86(5)	1.24(67)	8.38/1.78
60022-01-04-02	52103.685	1.0(1)	2.87(6)	-0.1(1)	10.68(9)	1.20(7)	4.01(9)	7.03(3)	0.50(5)	1.63(3)	1.04(67)	7.78/1.72
60022-01-01-07	52127.54	0.99(3)	2.53(7)	0.24(1)	13.08(3)	1.18(4)	2.64(9)	6.58(3)	0.36(8)	1.14(3)	1.10(67)	8.71/2.21
60022-01-03-03	52128.667	0.99(5)	2.78(5)	-0.26(5)	10.23(1)	1.20(8)	6.8(1)	6.34(5)	0.4(1)	1.57(3)	1.04(67)	8.24/1.94
60022-01-04-04	52128.734	1.0(1)	2.93(5)	-0.29(8)	10.40(7)	1.20(9)	5.8(1)	7.09(4)	0.38(7)	1.65(4)	1.05(67)	8.04/1.96
60022-01-03-04	52129.386	1.02(6)	2.72(6)	-0.17(7)	9.9(1)	1.20(4)	5.97(9)	6.42(3)	0.37(8)	1.83(3)	1.01(67)	8.38/1.86
60022-01-04-01	52131.114	1.07(6)	2.87(6)	-0.3(1)	9.36(3)	1.20(8)	4.56(6)	7.09(5)	0.46(6)	1.64(4)	1.15(67)	7.15/1.53
60022-01-05-00	52131.507	1.0(1)	2.62(5)	-0.09(1)	8.5(1)	1.30(6)	5.8(1)	5.99(7)	0.47(4)	1.69(3)	1.16(67)	7.49/1.60
60022-01-05-01	52131.375	0.99(7)	2.89(8)	-0.36(1)	8.2(1)	1.20(4)	6.5(1)	5.98(7)	0.41(8)	1.72(6)	1.05(67)	7.61/1.64
60022-01-06-01	52166.493	1.0(1)	2.75(3)	-0.17(2)	11.19(5)	1.20(9)	5.53(5)	5.87(7)	0.43(9)	1.61(3)	0.96(67)	8.73/2.13
60022-01-06-03	52168.754	1.00(7)	2.96(6)	-0.37(5)	11.36(6)	1.2(1)	5.52(9)	5.57(8)	0.39(4)	1.63(3)	1.16(67)	8.76/2.05

Table 4—Continued

Observational ID	MJD, day	$\alpha =$ $\Gamma - 1$	$T_e$ , keV	$\log(A)$	$N_{COM}^{\dagger\dagger}$	$T_s$ , keV	$N_{Bbody}^{\dagger\dagger}$	$E_{line}$ , keV	$\sigma_{line}$ , keV	$N_{line}^{\dagger\dagger}$	$\chi_{red}^2$ (d.o.f.)	$F_1/F_2^{\dagger\dagger\dagger}$
60022-01-06-05	52169.610	1.01(4)	2.65(4)	0.08(7)	11.04(7)	1.20(5)	5.26(8)	6.17(3)	0.418	1.65(6)	1.06(67)	8.34/2.31
60022-01-06-06	52169.678	1.02(5)	3.04(6)	-0.40(3)	12.17(8)	1.20(9)	5.22(7)	6.28(2)	0.38(6)	1.63(8)	1.11(67)	8.94/2.20
60022-01-06-07	52170.534	1.03(5)	2.6(1)	-0.04(3)	7.20(4)	1.20(5)	5.33(3)	6.47(7)	0.50(8)	1.68(7)	1.12(67)	6.58/1.38
60022-01-06-00	52170.983	1.00(5)	2.65(7)	-0.15(5)	9.4(1)	1.30(6)	6.53(7)	5.87(6)	0.39(7)	1.64(4)	1.1(67)	7.98/1.72
60022-01-06-09	52171.194	1.06(7)	2.86(5)	-0.23(4)	11.1(1)	1.20(7)	5.70(5)	6.47(8)	0.37(9)	1.74(5)	1.06(67)	8.75/2.13
60022-01-06-08	52172.176	1.04(4)	2.99(8)	-0.43(6)	10.40(5)	1.20(9)	5.39(6)	6.57(6)	0.4(1)	1.71(4)	1.1(67)	8.22/1.82
60022-01-06-10	52172.241	1.0(1)	2.66(4)	-0.25(5)	10.03(4)	1.20(5)	6.26(8)	6.43(7)	0.40(8)	1.68(3)	0.95(67)	8.44/2.02
60022-01-06-11	52172.725	0.99(6)	2.62(9)	-0.49(7)	9.34(5)	1.30(6)	6.34(5)	6.40(3)	0.38(7)	1.74(2)	1.08(67)	8.30/1.83
60022-01-06-12	52172.792	1.00(3)	3.41(9)	-0.54(4)	12.08(7)	1.20(8)	5.24(9)	6.81(5)	0.35(8)	1.81(5)	1.01(67)	8.84/2.15
60022-01-06-13	52172.852	1.03(5)	2.83(3)	-0.20(3)	11.63(6)	1.20(5)	6.09(9)	6.17(7)	0.32(5)	1.77(7)	1.05(67)	8.88/2.24
60022-01-07-00	52201.445	1.04(4)	2.75(5)	-0.13(3)	10.13(3)	1.20(6)	5.50(8)	6.24(8)	0.35(8)	1.69(3)	1.07(67)	8.06/1.98
60022-01-07-02	52204.424	1.06(9)	2.75(5)	-0.23(6)	9.11(4)	1.20(5)	5.42(9)	6.36(6)	0.3(1)	1.65(4)	0.89(67)	7.57/1.67
60022-01-07-03	52207.202	1.03(5)	2.76(3)	-0.02(1)	11.05(5)	1.20(7)	5.07(9)	5.85(7)	0.35(8)	1.62(3)	1.15(67)	8.31/2.32
60022-01-07-04	52207.071	1.01(4)	2.69(3)	-0.01(1)	10.37(3)	1.20(3)	5.56(8)	6.52(5)	0.4(1)	1.76(5)	1.12(67)	8.26/2.06
60022-01-08-00	52230.164	1.0(5)	2.58(4)	-0.01(1)	7.64(1)	1.3(1)	5.67(7)	5.87(7)	0.50(9)	1.64(3)	1.15(67)	6.84/1.49
60022-01-09-00	52295.306	1.0(4)	2.51(4)	0.23(1)	12.25(4)	1.2(1)	3.53(8)	5.97(8)	0.46(8)	1.67(6)	1.14(67)	8.55/2.04
60022-01-10-00	52321.559	1.0(5)	2.50(4)	0.11(1)	13.26(4)	1.20(9)	2.71(8)	5.85(9)	0.41(6)	1.71(8)	1.2(67)	8.72/1.97
60022-01-10-01	52320.301	1.0(6)	2.51(2)	0.09(1)	13.77(1)	1.20(6)	2.61(8)	5.78(7)	0.46(7)	1.61(4)	1.1(67)	9.08/2.18
60022-01-10-02	52320.876	1.0(3)	2.52(1)	0.06(1)	12.19(4)	1.20(5)	2.60(8)	5.87(6)	0.4(1)	1.65(4)	1.04(67)	8.01/1.76
60022-01-10-03	52324.647	0.99(2)	2.44(2)	0.14(5)	11.36(4)	1.10(8)	1.57(6)	6.26(6)	0.47(9)	1.87(3)	1.11(67)	6.39/1.37
60022-01-10-04	52325.760	0.99(2)	2.44(3)	0.15(6)	11.91(5)	1.10(9)	2.23(6)	6.47(7)	0.51(6)	1.79(6)	1.09(67)	6.39/1.37
60022-01-08-00	52230.164	1.00(5)	2.58(4)	-0.02(1)	7.64(2)	1.2(1)	5.67(7)	6.75(6)	0.53(8)	1.86(4)	0.88(67)	6.84/1.49
60022-01-11-00	52356.747	0.99(3)	2.50(2)	0.08(7)	9.94(6)	1.10(8)	1.29(6)	6.55(4)	0.49(6)	1.86(7)	1.2(67)	6.39/1.37
60022-01-11-01	52356.814	0.99(1)	2.47(1)	0.12(4)	11.79(3)	1.10(5)	1.58(6)	6.46(3)	0.5(1)	1.85(7)	1.15(67)	7.54/1.64
60022-01-11-03	52357.083	0.99(2)	2.41(1)	0.6(1)	13.29(4)	1.10(8)	2.8(1)	6.57(7)	0.50(9)	1.87(4)	1.1(67)	8.56/1.94
60022-01-11-02	52394.572	1.0(1)	2.51(2)	0.41(4)	12.56(4)	1.10(4)	6.2(1)	6.38(5)	0.39(7)	1.94(3)	1.19(67)	9.92/2.36
60022-01-12-00	52394.891	1.0(1)	2.73(4)	0.08(7)	13.26(7)	1.10(7)	5.76(8)	6.49(9)	0.37(8)	1.85(6)	1.01(67)	9.92/2.36





Table 4—Continued

Observational ID	MJD, day	$\alpha =$ $\Gamma - 1$	$T_e,$ keV	$\log(A)$	$N_{COM}^{\dagger\dagger}$	$T_s,$ keV	$N_{Bbody}^{\dagger\dagger}$	$E_{line},$ keV	$\sigma_{line},$ keV	$N_{line}^{\dagger\dagger}$	$\chi_{red}^2$ (d.o.f.)	$F_1/F_2^{\dagger\dagger\dagger}$
60022-01-13-00	52554.152	1.0(1)	2.46(2)	0.6(1)	12.5(9)	1.1(1)	9.48(4)	6.35(5)	0.35(4)	1.91(4)	1.07(67)	9.92/2.36
60022-01-13-01	52554.484	1.00(5)	2.56(5)	0.03(1)	13.6(7)	1.20(5)	2.85(7)	6.48(7)	0.36(9)	1.86(3)	1.16(67)	8.87/1.99
90022-05-01-00	53108.101	1.04(8)	2.42(9)	-0.18(6)	4.22(3)	1.5(1)	4.07(3)	6.38(6)	0.53(2)	0.87(5)	1.36(67)	3.85/0.79
90022-05-01-01	53108.256	1.00(8)	3.1(1)	-0.46(7)	4.75(7)	1.59(9)	3.68(5)	6.34(5)	0.60(8)	1.03(7)	1.38(67)	3.99/0.84
90022-05-02-00	53238.243	1.01(8)	2.56(4)	0.10(6)	4.20(7)	1.19(7)	2.58(9)	6.39(9)	0.62(3)	0.77(9)	1.34(67)	3.07/0.64
90022-05-03-00	53245.990	1.06(9)	2.36(2)	0.30(6)	5.42(5)	1.19(8)	1.5(1)	6.5(1)	0.6(1)	0.79(8)	1.00(67)	3.76/0.75
90022-05-04-00	53252.490	1.00(4)	2.5(1)	0.10(7)	6.05(9)	1.19(6)	1.51(8)	6.6(1)	0.65(8)	0.86(9)	1.00(67)	3.11/0.83
90022-05-04-01	53253.859	1.0(1)	2.47(2)	0.06(2)	6.08(3)	1.50(6)	2.49(5)	6.50(9)	0.66(6)	0.83(5)	1.25(67)	4.23/0.85
90022-05-05-00	53263.468	1.01(4)	2.52(1)	0.04(1)	5.33(2)	1.50(8)	2.24(2)	6.49(7)	0.67(8)	0.97(7)	1.15(67)	4.23/0.85
90022-05-06-00	53265.412	1.09(6)	2.52(2)	0.01(1)	5.42(3)	1.45(7)	2.46(3)	6.6(1)	0.63(6)	0.87(5)	1.15(67)	3.78/0.75
90022-05-06-01	53265.541	1.0(1)	2.50(1)	0.01(1)	5.56(5)	1.39(5)	2.08(4)	6.62(9)	0.62(4)	0.79(7)	1.05(67)	3.79/0.77
90022-05-06-02	53265.675	1.01(2)	2.51(2)	0.04(2)	5.54(6)	1.41(4)	2.34(6)	6.67(5)	0.61(8)	0.79(5)	1.07(67)	3.82/0.78
90022-05-06-03	53265.806	1.02(5)	2.56(2)	-0.02(1)	4.98(3)	1.6(1)	2.22(5)	6.6(1)	0.62(9)	0.81(9)	1.08(67)	3.44/0.69
90022-05-07-00	53279.124	1.00(7)	2.53(1)	0.10(6)	3.53(1)	1.70(8)	2.45(3)	6.64(7)	0.64(5)	0.85(6)	1.18(67)	3.44/0.69
90022-05-07-00	53280.960	1.03(9)	2.42(1)	0.31(3)	5.42(3)	1.50(9)	2.18(3)	6.65(8)	0.62(8)	0.79(7)	0.97(67)	3.44/0.69
94307-05-01-00	55129.659	1.02(3)	3.16(4)	0.41(3)	4.53(7)	1.4(1)	3.08(2)	6.58(2)	0.4(1)	0.32(1)	1.09(67)	3.21/1.28
94307-05-01-000	55440.307	1.04(4)	3.16(5)	0.45(4)	4.53(7)	1.50(8)	3.08(3)	6.59(5)	0.40(7)	0.34(2)	0.87(67)	3.21/1.28
94307-05-01-00	55440.62	1.03(8)	2.50(2)	0.25(2)	4.67(2)	1.4(1)	4.17(4)	6.64(9)	0.62(9)	0.68(9)	1.13(67)	3.78/0.78
94307-05-01-01	55440.701	1.03(9)	3.16(4)	0.41(3)	4.53(7)	1.40(6)	3.08(2)	6.58(3)	0.4(1)	0.32(6)	0.89(67)	3.21/1.28
94307-05-01-02	55440.766	1.02(3)	3.26(7)	-0.56(3)	4.57(1)	1.35(7)	4.13(2)	6.21(2)	0.5(1)	0.21(7)	0.98(67)	3.21/1.28

<sup>†</sup> The spectral model is  $wabs * (blackbody + COMPTB + Gaussian)$ , where  $N_H$  is fixed at a value  $1.6 \times 10^{22} \text{ cm}^{-2}$  (Oosterbroek et al., 2000); color temperature  $T_{BB}$  is fixed at 0.6 keV (see comments in the text); <sup>††</sup> normalization parameters of *blackbody* and *COMPTB* components are in units of  $L_{37}^{soft}/d_{10}^2$ , where  $L_{37}^{soft}$  is the source luminosity in units of  $10^{37} \text{ erg/s}$ ,  $d_{10}$  is the distance to the source in units of 10 kpc and *Gaussian* component is in units of  $10^{-2} \times \text{total photons cm}^{-2} \text{ s}^{-1}$  in line, <sup>†††</sup>spectral fluxes ( $F_1/F_2$ ) in units of  $\times 10^{-9} \text{ ergs/s/cm}^2$  for (3 – 10) and (10 – 50) keV energy ranges respectively.

Table 5. Comparisons of the best-fit parameters of atoll sources GX 3+1 and 4U 1728-34<sup>1</sup>

Source name	Alternative name	Class <sup>2</sup>	Distance, kpc	Presence of kHz QPO	$kT_e$ , keV	$N_{COM}$ $L_{39}^{soft}/D_{10}^2$	$kT_{BB}$ , keV	$kT_s$ , keV	$f$
4U 1744-26	GX 3+1	Atoll, Sp, B	4.5 <sup>3</sup>	none <sup>5</sup>	2.3-4.5	0.04-0.15	0.6	1.16-1.7	0.2-0.9
4U 1728-34	GX 354-0	Atoll, Su, D	4.2-6.4 <sup>4</sup>	+ <sup>6</sup>	2.5-15	0.02-0.09	0.6-0.7	1.3	0.5-1

References: (1) ST11, (2) Classification of the system in the various schemes (see text): Sp = supercritical, Su = subcritical, B = bulge, D = disk, (3) Kuulkers & van der Klis (2000), (4) van Paradijs (1978), (5) Strohmayer (1998) (6) Titarchuk & Osherovich (1999)

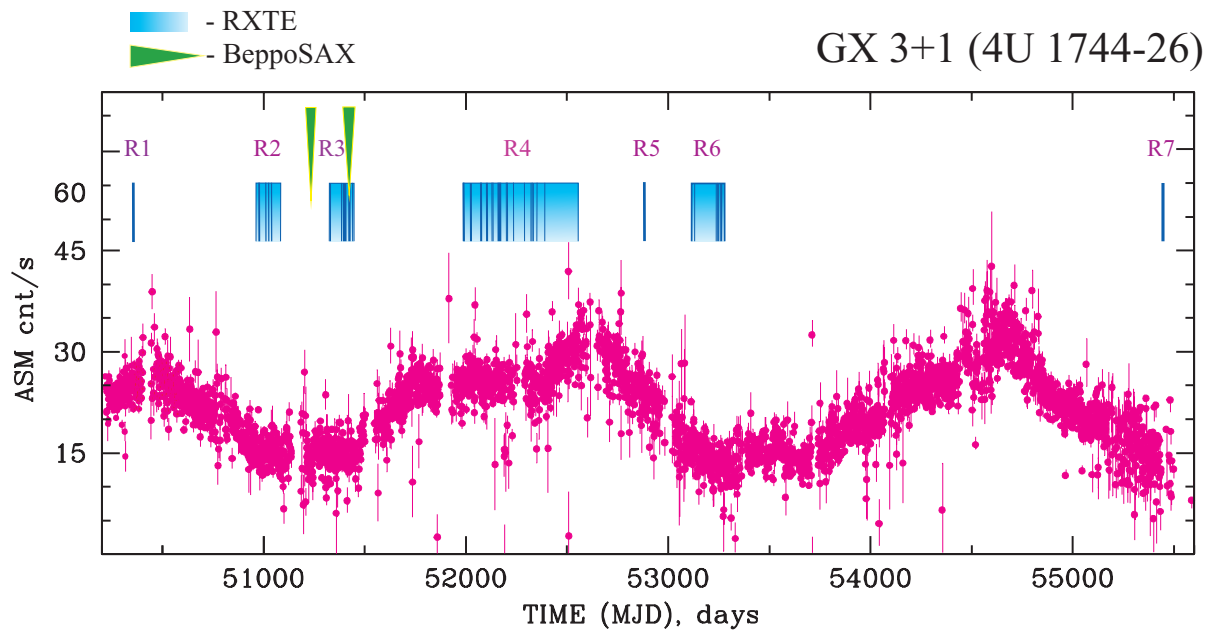


Fig. 1.— Evolution of ASM/*RXTE* count rate during 1996 – 2010 observations of GX 3+1. *Blue* vertical strips (*on the top of the panel*) indicate to time for the *RXTE* pointed observations. Whereas *bright blue* rectangles are related to the *RXTE* data sets listed in Table 1, *green* triangles show *BeppoSAX* NFI data, listed in Table 2.

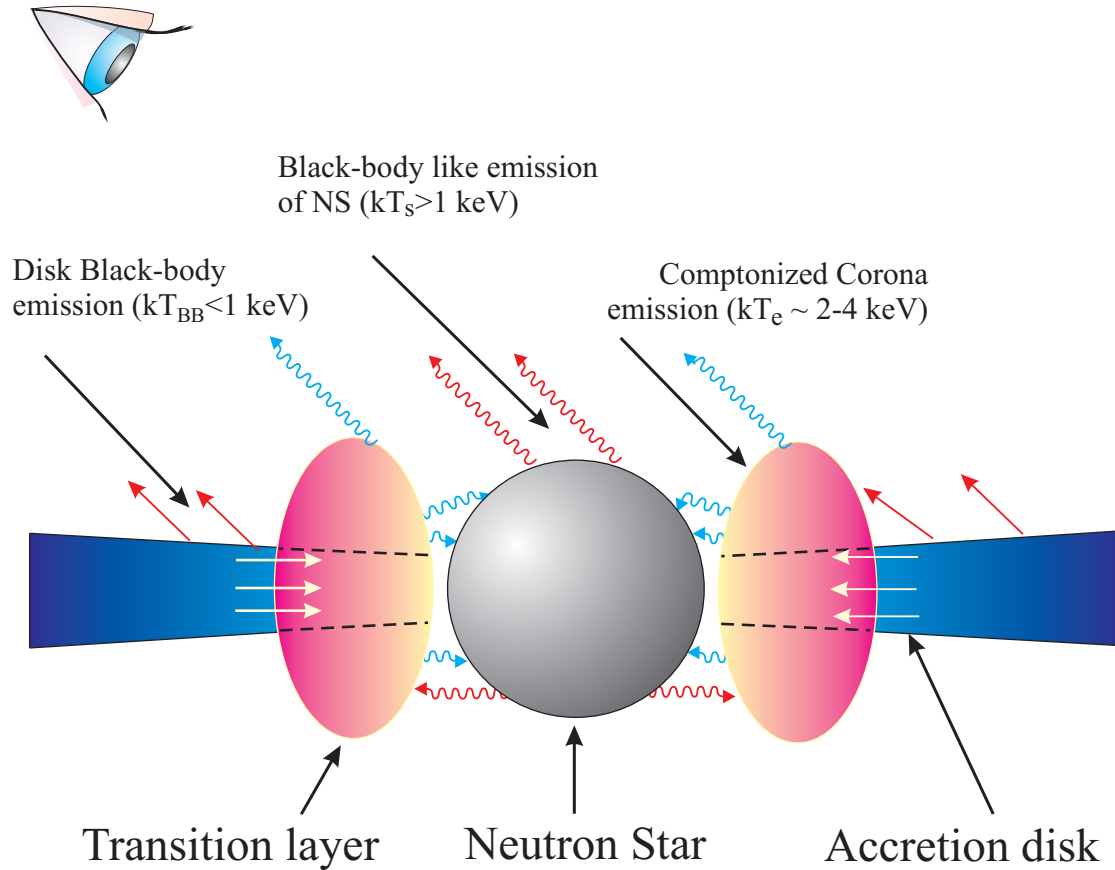


Fig. 2.— A suggested geometry of GX 3+1. Disk and neutron star soft photons are up-scattered off hotter plasma of the transition layer located between the accretion disk and NS surface. Some fraction of these photons is seen directly by the Earth observer. Red and blue photon trajectories correspond to soft and hard (upscattered) photons respectively.

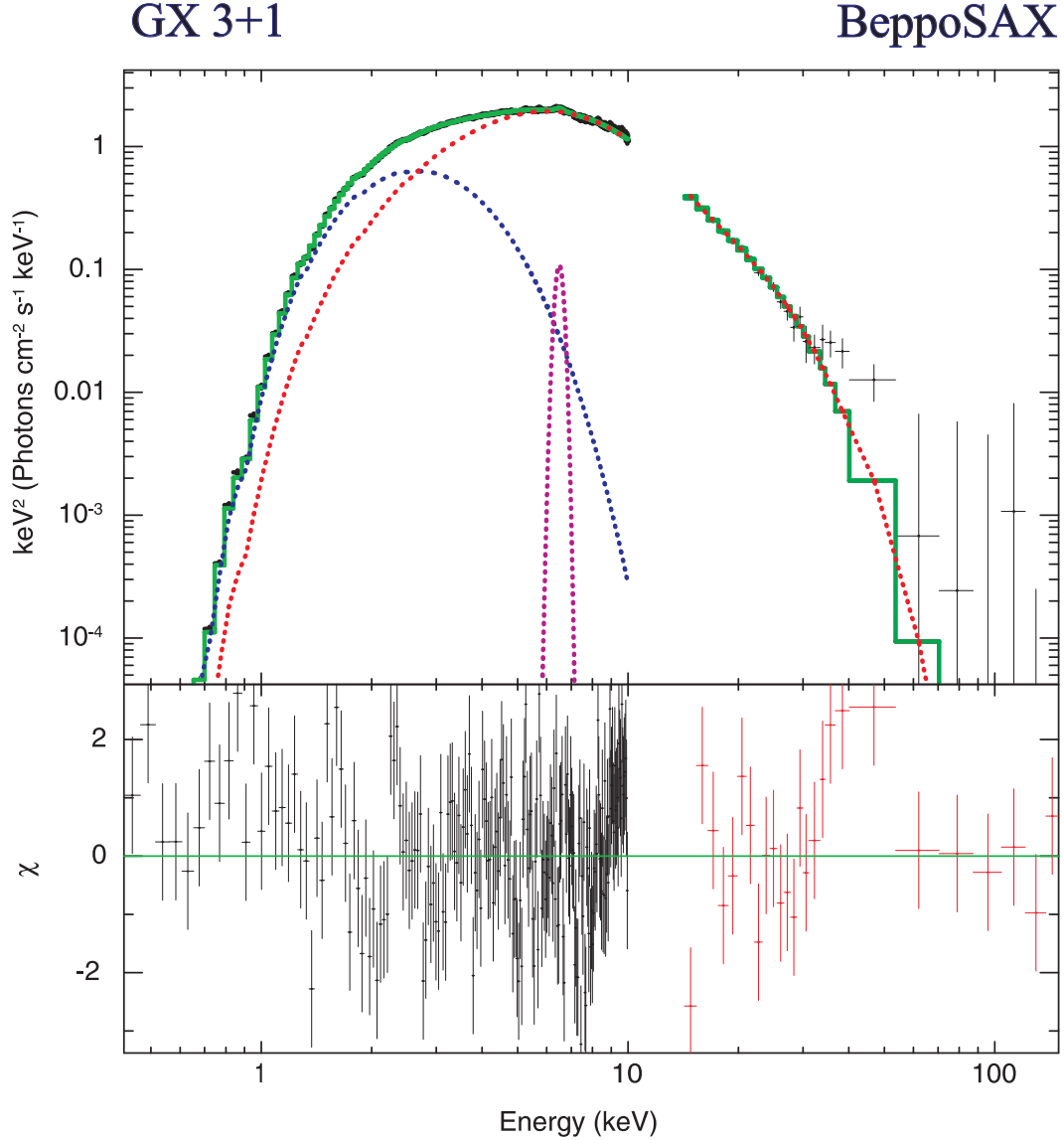


Fig. 3.— *Top* : the best-fit spectrum of GX 3+1 in  $E * F(E)$  units using *BeppoSAX* observation 20603001 carried out on 28 February – 1 March 1999. The data are presented by crosses and the best-fit spectral model  $wabs*(blackbody+COMPTB+Gaussian)$  by green line. The model components are shown by blue, red and crimson lines for *blackbody*, *COMPTB* and *Gaussian* components respectively. *Bottom*:  $\Delta\chi$  vs photon energy in keV. The best-fit model parameters are  $\Gamma=1.99\pm 0.07$ ,  $T_e=3.68\pm 0.05$  keV and  $E_{line}=7.4\pm 0.1$  keV (reduced  $\chi^2=1.08$  for 457 d.o.f) (see more details in Table 3).

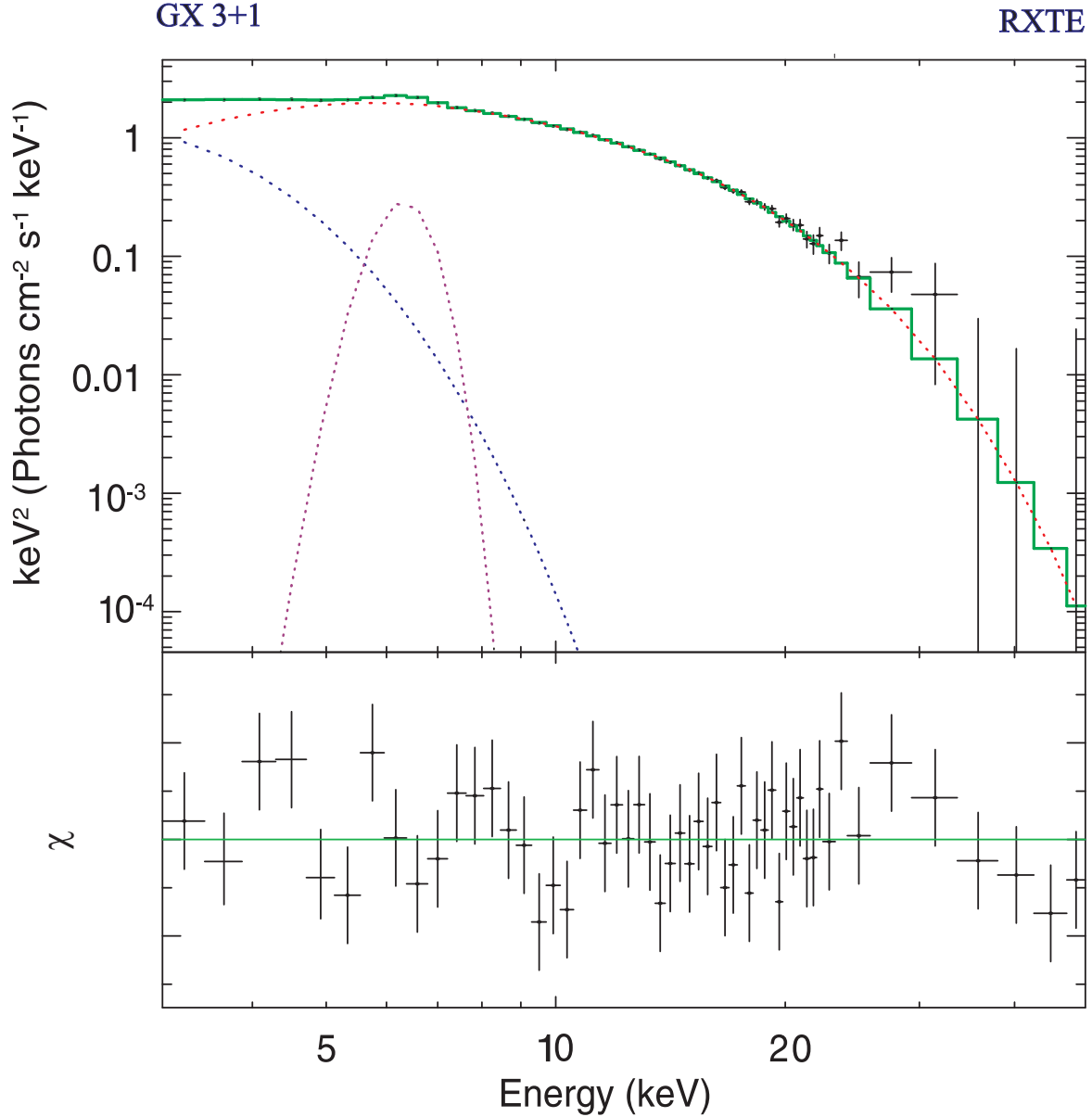


Fig. 4.— *Upper panel:* A typical  $E * F(E)$  spectral diagram of GX 3+1 for PCA/RXTE observation 94307-05-01-000 on 2010, 1 September (MJD 55431.62) during the *faint* phase (green line). The spectral model, presented by its components is shown by dashed red, blue, and purple lines for *COMPTB*, *blackbody* and *Gaussian* components respectively. *Bottom panel:*  $\Delta\chi$  vs photon energy in keV. The best-fit model parameters are  $\Gamma = 2.04 \pm 0.04$ ,  $kT_e = 3.16 \pm 0.05$  keV and  $E_{line} = 6.59 \pm 0.05$  keV (reduced  $\chi^2 = 0.87$  for 67 d.o.f.) (see more details in Table 4).

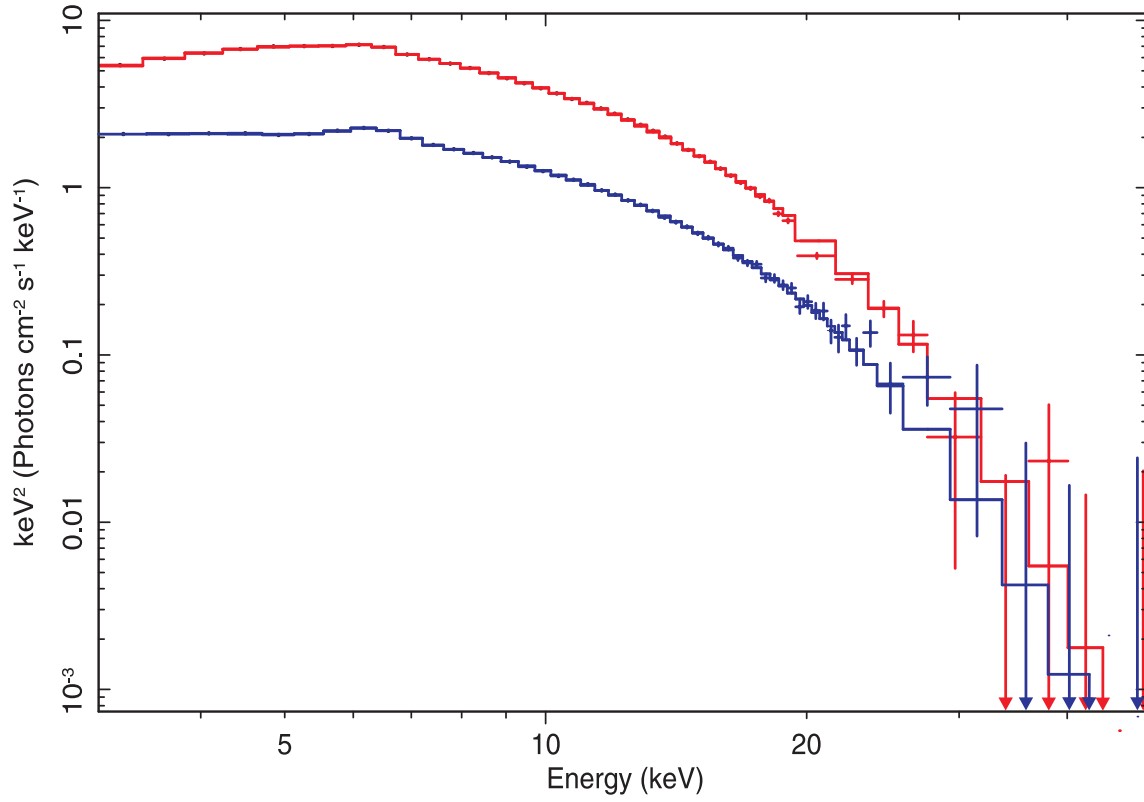


Fig. 5.— Examples of X-ray spectra, presented as  $E * F(E)$  spectral diagrams, of GX 3+1 during *faint* phase (94307-05-01-00, *blue*) and *bright* phase (60022-01-13-01, *red*) detected with *RXTE* on MJD 55440.62 and 52544.48 respectively.



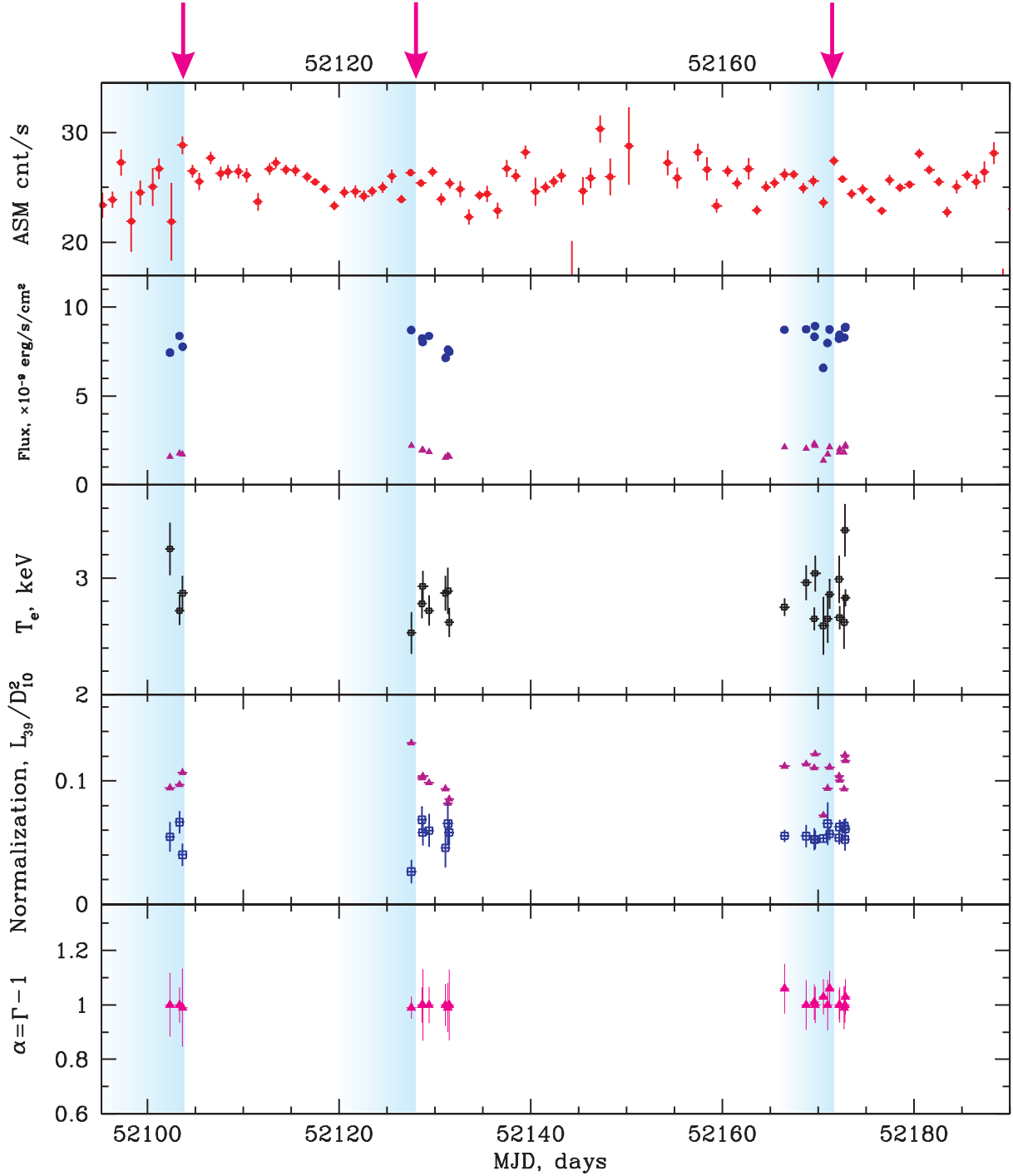


Fig. 6.— *From Top to Bottom:* Evolutions of the ASM/*RXTE* count rate, model flux in 3-10 keV and 10-60 keV energy ranges (*blue* and *crimson* points respectively), electron temperature  $T_e$  in keV, *COMPTB* and *blackbody* normalizations (*crimson*, *blue* points respectively) and spectral index  $\alpha = \Gamma - 1$  during 2001–2002 outburst transitions set ( $R_4$ ). The rising phases of the *mild* transition are marked with blue vertical strips. The peak burst times are indicated by the arrows on the top of the plot.

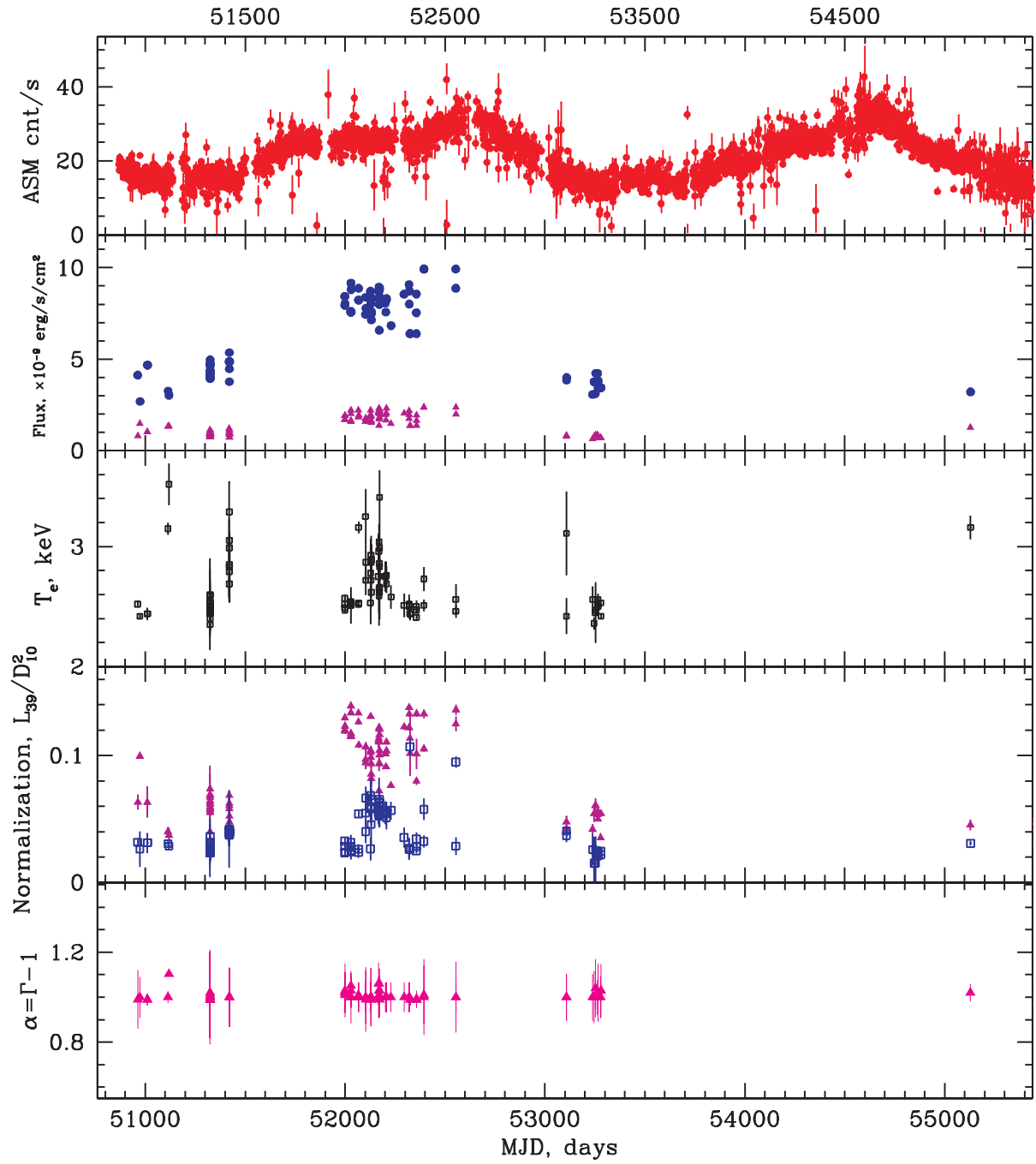


Fig. 7.— Same to that presented in Fig. 6 but for all the *RXTE* sets (*R1 - R7*) to demonstrate *slow* (*long - term*) variability.

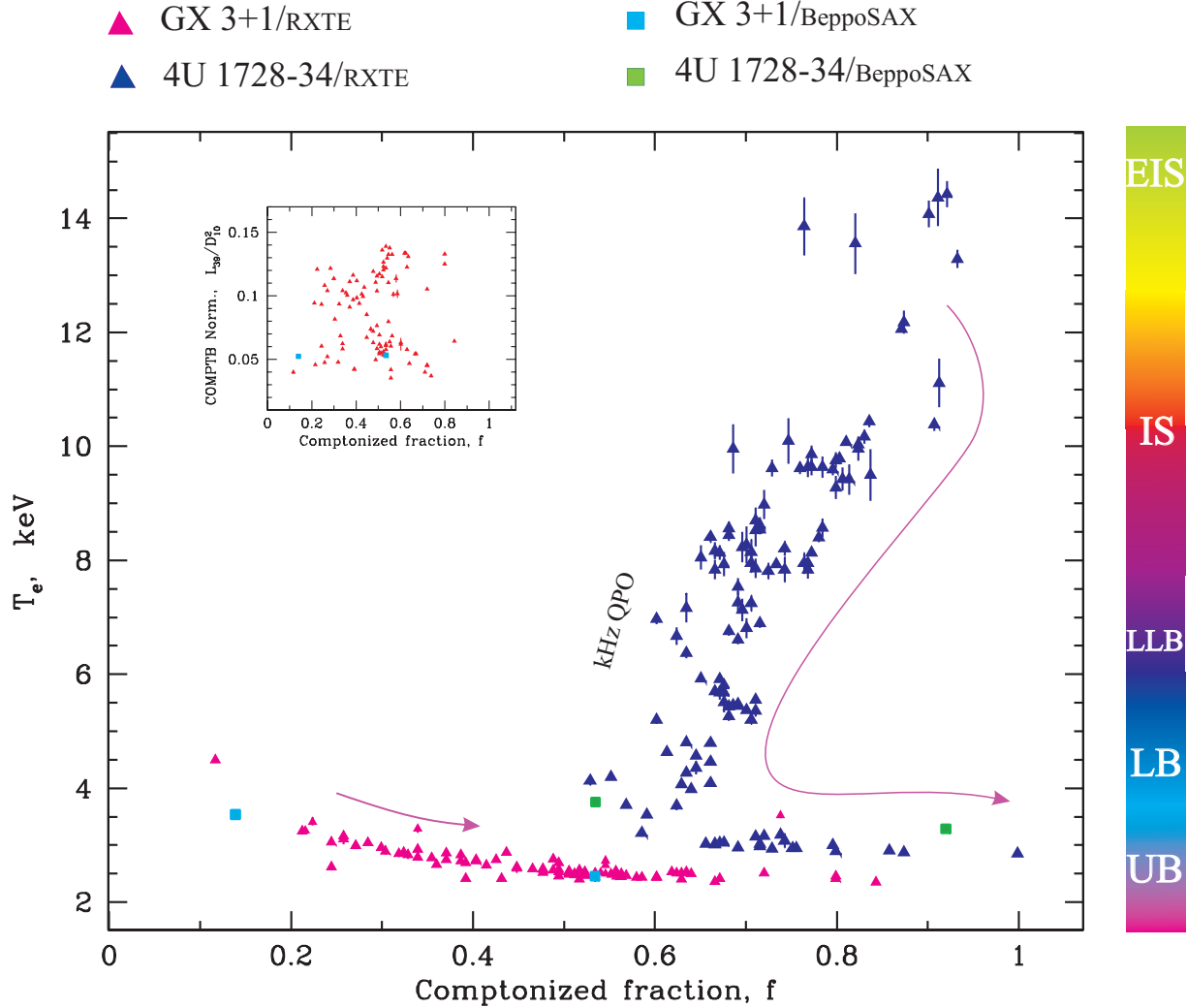


Fig. 8.— Electron temperature  $T_e$  (in keV) plotted versus illumination fraction  $f = A/(1 + A)$  for atoll sources GX 3+1 and 4U 1728-34 during *mild* variability. *Pink/bright blue* and *blue/green* points correspond to *RXTE/BeppoSAX* observations of GX 3+1 and 4U 1728-34 respectively. For GX 3+1 COMPTB normalization measured in  $L_{39}^{soft}/D_{10}^2$  units versus illumination fraction  $f$  is plotted in the *incorporated panel (top left)* during long-term (*slow*) variability (see Table 4). The *bended arrows* are related to an increase of mass accretion rate. On the right-hand side we show a sequence of CD states (EIS – the extreme island state, IS – island state, LLB – lower left banana state, LB – lower banana state and UB – upper banana state) which are listed according to the standard atoll-Z scheme (Hasinger & van der Klis 1989). One can see that  $T_e$  is directly related with the sequence of CD states. Along the track for 4U 1728-34 we indicate points of  $T_e - f$  correlation where kHz QPOs are detected.

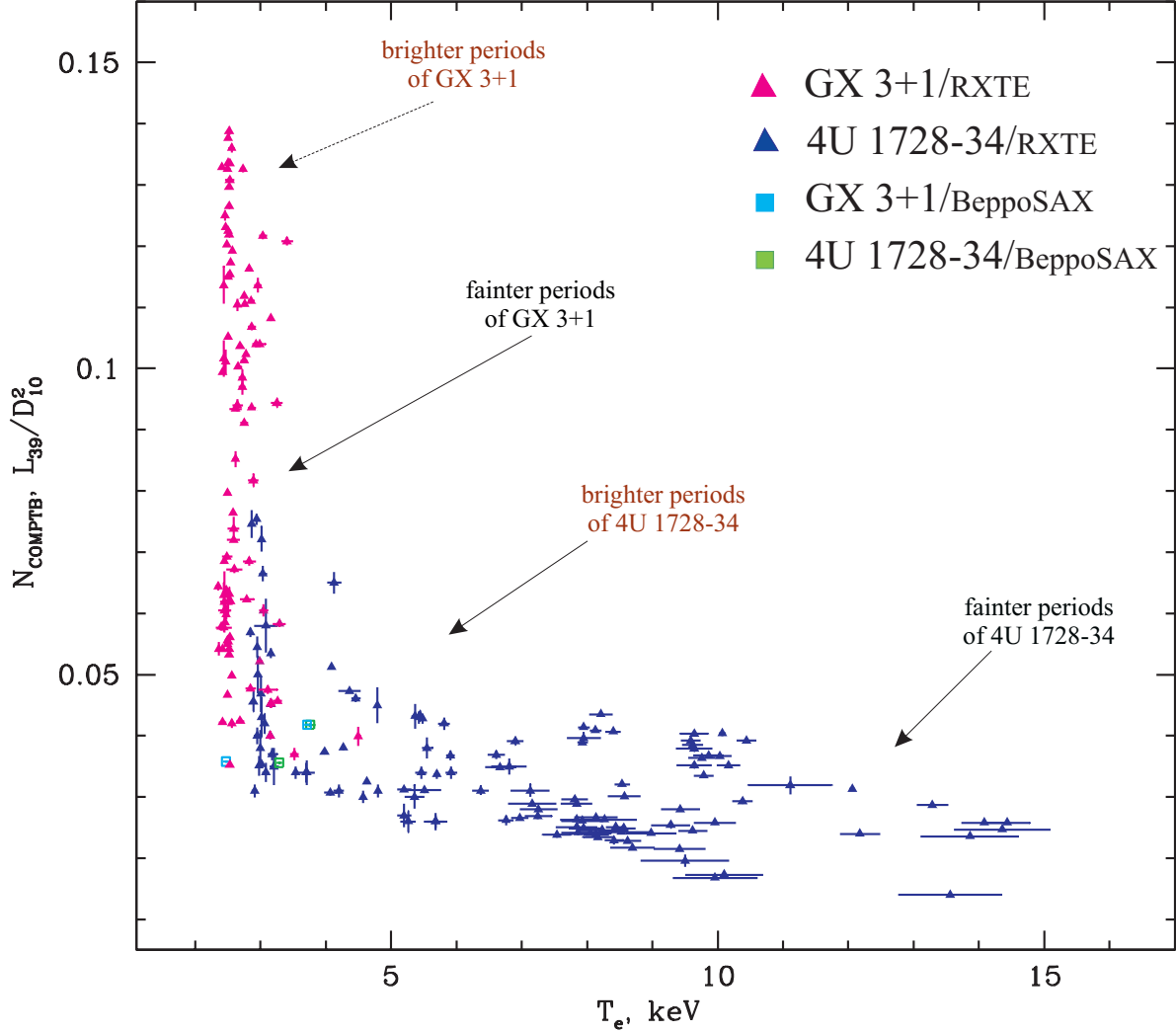


Fig. 9.— COMPTB normalization measured in  $L_{39}^{soft}/D_{10}^2$  units versus electron temperature  $T_e$  (in keV) obtained using the best-fit spectral model  $wabs * (blackbody + COMPTB + Gaussian)$  for *atoll* sources GX 3+1 (*pink*) and 4U 1728-34 (*blue*, taken from ST11) for *RXTE* data and *bright blue* and *green* points for *BeppoSAX* data. Mass accretion rate continuously increases along this correlation from the right to the left.

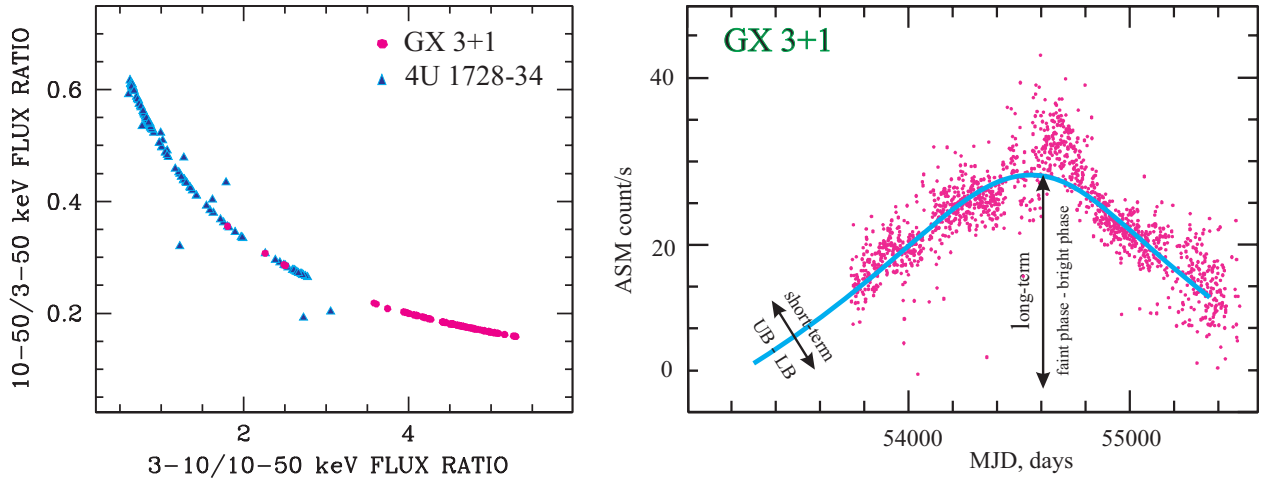


Fig. 10.— *Left:* The *color-color diagram* [3 – 10/10 – 50 keV flux ratio versus 10 – 50/3 – 50 keV flux ratio] of GX 3+1 (*pink*) and 4U 1728-34 (*blue*) during faint-bright transitions (long-term variability). *Right:* Fragment of ASM light curve of GX 3+1 which shows two types of flux variability. One is a long-term trend (from faint to bright) related to COMPTB normalization changes and another one is short-term time variations (UB – LB) related to the electron temperature changes. The blue line presents a mean count rate and indicates to a long-term variability of GX 3+1.

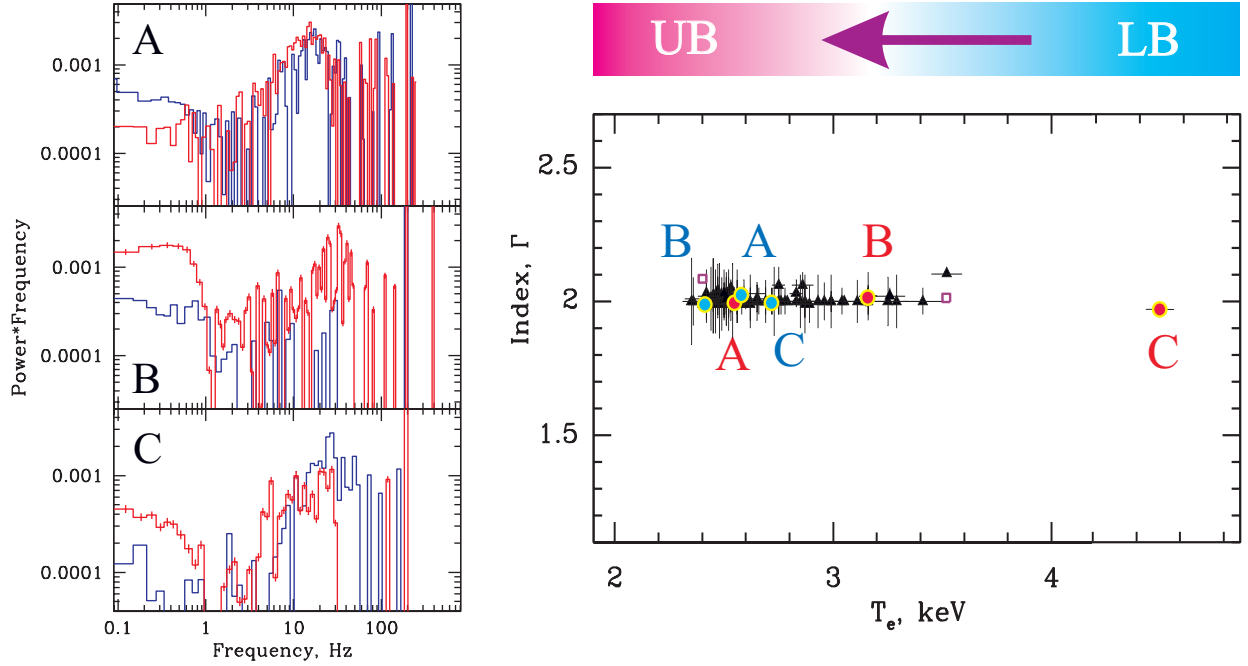


Fig. 11.— *Left column:* PDSs presented in terms of  $\nu P(\nu)$  for 13 – 30 keV energy band correspond to *lower banana* and *upper banana* states of GX 3+1 and related to different electron temperatures indicated by points A, B and C on the *right panel* of the Figure. The strong noise component HFN seen in the 1 – 50 Hz range and relatively weak VLFN at the frequencies below  $\sim 1$  Hz are present before and after transition (see panels A and C) from LB to UB. In UB (panel B, *blue* histogram) the power spectra of GX 3+1 are dominated by the VLFN with a break at about 20 Hz. *Right panel:* Photon index  $\Gamma$  plotted versus electron temperature  $T_e$  (in keV) using our spectral model *wabs\*(blackbody+COMPTB+Gaussian)* during spectral transitions (see Table 4). Violet and black points correspond to *BeppoSAX* and *RXTE* observations of GX 3+1 respectively. The violet arrow in *top part of the right panel* points the direction of LB $\rightarrow$ UB transition related to a decrease of  $T_e$ .